Spring 2009

Experiments and modeling of shear-driven film separation

J. L. Wegener

Department:

EXPERIMENTS AND MODELING OF SHEAR-DRIVEN FILM SEPARATION

by

JEFFREY LEWIS WEGENER

A THESIS

Presented to the Faculty of the Graduate School of the

MISSOURI UNIVERSITY OF SCIENCE AND TECHNOLOGY

In Partial Fulfillment of the Requirements for the Degree

MASTER OF SCIENCE IN MECHANICAL ENGINEERING

2009

Approved by

James A. Drallmeier, Advisor
Darryl J. Alofs
Bassem F. Armaly
Ralph W. Wilkerson

ABSTRACT

Dynamic thin liquid films driven by an adjacent gas flow have been subject to many investigations due to the presence of such films in many engineering applications. More specifically though, the behavior of such films at a sharply expanding corner has received little attention, but can be observed in internal combustion engines, liquid atomizer systems, refrigerant flows in evaporators, and film drag over wetted surfaces. Efforts to validate computational models of the propagation and separation of films are limited by the lack of reliable non-intrusive techniques to measure and analyze dynamic film parameters. In this study, film propagation models and film separation models were validated separately using experimental film thickness and separation measurements. These experimental measurements were performed in an experimental facility that enabled controlled development of a shear-driven thin liquid film and allowed for subsequent film analysis. For film thickness measurement, a laser focus displacement instrument was used following a theoretical and experimental qualification of the instrument. Thickness measurements with corresponding film velocities were then compared to the computational results of two numerical simulations. This comparison revealed inaccuracies within the computational results. The experimental facility was also used to measure film separation at a sharp corner. Two film separation models were validated using these measurements, and neither of the two models accurately predicted the onset of film separation for different film viscosities. Control variables include gas and film velocities, film flow rate, film viscosity, and film surface tension.

ACKNOWLEDGMENTS

Foremost, I would like to thank my advisor, Dr. James A. Drallmeier. Dr. Drallmeier taught two of my undergraduate courses, hired me as an undergraduate research assistant, and eventually as a graduate research assistant. By sacrificing excess time and energy he has made my academic experience both enjoyable and very progressive. Throughout my development as an undergraduate and graduate student, his experience and wisdom provided a superior learning environment. I would also like to express my thanks to the National Science Foundation for the financial support which has made my research possible. I am thankful for the encouragement and understanding of my family and friends throughout my academic career. Also, Dr. Thomas Schuman of the Missouri S&T Department of Chemistry was extremely helpful by allowing me to use his laboratory's tensiometer, which was a critical part of my experiment. Hai Lan, a former mechanical engineering PhD candidate, created the geometry model used within the FLUENT computations described in this thesis. Without his help, and the help of Magesh Thiruvengadam, the computational portion of this study would have been much more difficult. Last, I thank the staff of the Mechanical and Aerospace Engineering Department for their assistance in clerical work, equipment maintenance, and fabrication.

TABLE OF CONTENTS

LIST OF FIGURES

LIST OF TABLES

NOMENCLATURE

Symbol	Description
A	area
A_f	cross sectional film area
F_c	lower meniscus surface tension force
F_s	surface tension force
$\vec{F}_{ex}$	external force vector
$\vec{g}$	gravitational acceleration vector
h	thickness
h'	measured thickness
$\overline{h}$	mean thickness
h_f	film thickness
$\overline{h}_f$	average film thickness
I	light intensity
I_o	incident light intensity
I_r	reflected light intensity
i	computational grid node
k	turbulent kinetic energy
k_a	imaginary refractive index of aluminum
k_1	imaginary refractive index of dielectric medium
k_2	imaginary refractive index of conductive medium
L_b	ligament length
m_2	refractive index of conductive medium including imaginary part
n	integer number of measured values
n	refractive index
$\vec{n}$	unit vector
n_a	refractive index of aluminum
n_{air}	refractive index of air
n_o	refractive index of optical crown glass

n_s	refractive index of sapphire
n_w	refractive index of water
n_1	refractive index of dielectric medium
n_2	refractive index of conductive medium
P	power of light received
P_o	power of incident light
p	direction perpendicular to separating film
$\dot{Q}_f$	two-dimensional film flow rate
R	radius of laser beam
Re_f	film Reynolds number
t	direction tangential to separating film
U_g	gas phase velocity
u_f	film velocity
$\overline{u}_f$	average film velocity
$\vec{V}$	velocity vector
v_f	film velocity in y direction
W	weight
We_f	film Weber number
We_{rel}	relative Weber number
w_f	film width
w_{fo}	film injection width
x	streamwise direction
x_o	location of beam center
y	vertical direction
z	spanwise direction
α	surface angle
α_f	liquid volume fraction
β	separating ligament angle relative to horizontal
$\Delta\mu_f$	change in film viscosity
ε	dissipation

θ	test section corner angle relative to horizontal
θ_c	laser beam cone angle
θ_r	angle of reflected light
θ_1	angle of incident light
θ_2	angle of refracted light
μ	viscosity
μ_f	film viscosity
ρ	density of air
ρ	reflection coefficient
$\rho_{al/w}$	reflection coefficient for aluminum-air interface
ρ_f	film density
ρ_w	reflection coefficient for water-air interface
$\rho\perp$	reflection coefficient for light polarized with the electric field of light perpendicular to the plane
$\rho_{//}$	reflection coefficient for light polarized with the electric field of light parallel to the plane
σ	surface tension
σ	standard deviation
τ	shear stress
$\forall$	volume
$\dot{\forall}_f$	volumetric film flow rate
∂	partial derivative
®	registered trademark

1. INTRODUCTION

Gas-liquid flows have application in a multitude of engineering problems and as a result have been studied for many years. These two phase flows can involve quickly moving gases that affect adjacent liquid at the interface of the two fluids, resulting in an interaction between the gas and liquid flow. In the case of a quickly moving gas for example, this gas-liquid interaction often results in a swiftly moving liquid film located on the wall of the system, which is shear-driven by the adjacent gas flow. In certain conditions, this situation results in wavy liquid films that interact with the gas phase through atomization. Atomization of these films can be broken up into stages for detailed analysis. Liquid at the film's surface can evaporate into the adjacent gas flow through aerodynamic instabilities, or atomization may follow a stepped process. This begins with the separation of the film from the solid wall to form a suspended liquid sheet, then the break-up of the liquid sheet into ligaments and droplets, and finally the atomization of droplets.

The stage of this atomization process where the film separates from a solid surface has received little attention, but yet applies to several engineering problems. Separation of liquid films is encountered in fuel and air mixture preparation for spark ignition engines, as well as in atomizer design, refrigerant flows in evaporators, and wave plate mist eliminators. It is understood that the separation process more readily occurs where the film flows over sharp corners. Thus, the behavior of such films at sharp corners is critical, and as a result, most film separation situations and certainly all of the applications discussed here involve films flowing over sharp corners.

In a cold–start situation of a port fuel injection engine, for example, fuel will form a liquid film on the port walls and the top surfaces of intake valves. The fuel then enters the combustion chamber as a shear driven thin liquid film, and the fuel then has been observed to atomize in varying degrees with the air entering the cylinder, forming droplets and ligaments in the process. Fuel that does not atomize and enters the cylinder as a liquid film has been observed to cause unburned hydrocarbon emissions. As the fuel film travels into the combustion chamber the liquid flows past corners located at the end of the intake port and at the edge of the valve, and film separation at these corners occurs in varying degrees, which directly affects atomization.

Wavy liquid films in prefilming airblast atomizers have been subject to study due to the film behavior's direct influence on atomization. In prefilming airblast atomizers, liquid is introduced into an air stream, resulting in a shear-driven film. The film then is driven off the solid substrate at a sharp corner where an adjacent air stream is introduced to form a liquid-gas interface where a liquid-solid interface was located before the corner. After separating from the solid surface, the adjacent gas flows on both sides of the film contribute to atomization. Consequently, film separation results are a primary concern for atomization.

In a wave-plate mist eliminator, used in process industries such as the oil industry to separate liquid from a primary gas stream, behavior of liquid films at sharply expanding corners is critical. The primary gas flow is forced to travel through a channel containing a series of sharp bends where the droplets entrained in the gas flow follow trajectories that results in their collision with the channel walls. In this format, it is desired that the droplets will form liquid films that remain attached to the solid wall of

the wave-plate. If the liquid films negotiate the corners of the wave-plate and remain attached to the solid surface then gravity can aid the drainage of fluid from the gas flow, ultimately separating liquid from gas as desired. Proper modeling of film flow and the separation criterion of these films is critical to determine if certain conditions will give the desired drainage result. Parameters such as gas phase velocities, film flow rates, film thickness, and corner angle must be analyzed in detail to create such models.

Figure 1.1. Schematic of shear-driven film interaction with separated gas phase flow resulting in partial film separation from the substrate at the corner.

Due to the desire to accurately describe film behavior, there are numerous film studies and most of these studies focus on a particular area. This study is concerned with the behavior of films at a sharp corner, such as the situation shown in Figure 1.1. Consequently, analysis was performed regarding flow parameters immediately before the corner and immediately after the corner, focusing on the conditions causing film separation or lack thereof. In some cases, issues associated with flow development far before the corner were included, but this is only in order to accurately predict the flow conditions immediately before the corner.

Experimental measurements of film thickness and film separation at a sharp corner for shear-driven films are presented, and consequently, the review of literature in Section 2 addresses film thickness measurement techniques and film separation studies. The film thickness measurement technique chosen for this study is critically examined in Section 3, including theoretical and experimental work to quantify the limitations of the technique. Section 4 describes the experimental facility, presents measured film thickness and separation data, and compares the results with previous models. Conclusions are made in Section 5 and recommendations are discussed in Section 6. Lastly, Appendix A contains data, derivations, and a computer code. Appendix B contains equipment and fluid specifications.

2. LITERATURE REVIEW

In order to establish a firm background of liquid film research the review of literature has been divided into two sections by their relation to this study. First, film thickness measurement techniques will be discussed including brief theoretical explanations and the applications of each technique. Second, the limited number of studies concerning liquid film separation will be discussed.

2.1. FILM THICKNESS MEASUREMENT TECHNIQUES

A multitude of investigations have been performed involving film thickness measurements. These studies have used many different techniques, often based in the realms of electricity or optics. For a long time, needle contact methods and fluid conductance methods were the most popular modes of measuring film thickness, as discussed by Hewitt [1]. But, these techniques are intrusive to the behavior of the film due to the needle contact point on the film surface or the meniscus formation at the wire-film interface in the case of conductance methods. As a result, a generation of non-intrusive film measurement techniques developed. This series of techniques is based in the field of optics. Fundamental knowledge of light absorption and reflection coupled with innovations in lasers and imaging technology has been used to develop several non-intrusive thickness measurement techniques, and these techniques will now be discussed.

Laser-induced fluorescence (LIF) has been utilized by many investigators for measuring film thickness. This technique uses an added dopant or the fluorescent components in the liquid as a source of fluorescence, which is induced by laser light often in the form of a laser sheet. This is a nonintrusive method, which is common to all of the

film thickness measuring techniques mentioned in this literature review. The laser-induced fluorescence is captured by an imaging device, obtaining 2-dimensional images which are then used to quantify film thickness.

Ting [2] studied engine lubricant film thickness around engine rings using laser-induced fluorescence with fiber optics. The laser light was projected through a transparent portion of the cylinder liner onto the piston ring, measuring the thickness of oil in between. The study explained the benefits of the method as compared to optical laser interferometry when applied to lubricant thickness measuring, mainly discussing surface finish requirements. Lubricating oil inherently contains sources of fluorescence, but a red fluorescent dye was added to enhance oil fluorescence. A calibration method was described but is not implemented, and only the signal traces, not quantitative data, was presented.

Shaw II et al. [3] also used laser-induced fluorescence to measure lubricant thickness on piston rings. The beam spot size was approximately 50 μm, which was a small proportion of the piston ring widths of 1 mm. A fluorescent dye, Coumarin 523, was used in concentrations of 10^{-4} mol/liter, which is claimed to be low enough to maintain the lubricant's rheology. The study's goals were to increase the robustness of this popular lubricant thickness measuring technique by increasing spatial resolution, improving signal to noise ratio, and validating the use of fiber optics in this environment. These goals were achieved, resulting in more precise identification of important features around piston rings, extended application to higher engine temperatures, and easier experimental set up.

Driscoll et al. [4] investigated ways of refining the laser-induced fluorescence technique. Mainly, the study was aimed at perfecting the calibration processes, developing a method for correcting data, and ensuring repeatability. The shear-driven film of an airblast atomizer was measured on the prefilming surface, which is rather difficult to reach with a laser. A sophisticated laser light directing system was constructed involving a translating mirror and lens within the spray chamber of the airblast atomizer. The working fluid was water with a fluorescein dye additive. The laser beam spot diameter was 40 μm and the repeatability of the technique is better than ±10 μm.

Yang and Melton [5] worked towards the selection of an ideal dopant for laser-induced fluorescence, responding to problems experienced when dopants change film properties, thus impairing experiments. They focused on a certain seven qualities: significant absorption at an available laser wavelength, satisfactory quantum yield, good solubility in the fuel used, co-evaporation in the fuel, insensitivity to oxygen quenching, insensitivity to temperature changes, and ready availability. This study was driven by the problems caused in many experiments that use laser-induced fluorescence, but lack a suitable dopant. For 40-50 chemicals, the fluorescence spectra were measured and those chemicals having fluorescence spectra in the visible range were tested for oxygen quenching and temperature sensitivity. Ultimately, two fluorescent dopants, cyclohexanone and 2-methyl-cyclopentanone, were tested as fluorescent markers for quantitative 2-dimensional imaging of the thickness of automotive fuel films in the range of 0-1 mm. The study did not apply these chemicals in and engine environment and cautioned the use of these chemicals in engines for a few reasons. Particularly, the chemicals studied may not provide for normal engine operation. Also, when the laser-

induced fluorescence technique is used in an engine, the other fluids present, such as oil and fuel, may contain fluorescent materials. Users must test for the background signals from these other sources and minimize interference.

Maroteaux et al. [6] performed a study on the separation of shear-driven thin liquid films at a sharp expanding corner, and because film thicknesses in such studies are critical, a laser-induced fluorescence method was used. Film thickness at the corner was estimated by measuring film thickness just upstream from the corner. A green dye which is used in commercial unleaded gasoline was added to dodecane as a source of fluorescence. Before making dynamic film thickness measurements the measurement accuracy was confirmed in a static environment, where thicknesses of 20-100 μm yielded an accuracy of ±3 μm. Two gas flows were tested: 60 m/s and 80 m/s, which resulted in film thicknesses of 10-30 μm.

Schagen and Modigell [7] used laser-induced fluorescence in an experimental facility designed for simultaneous measurement of film thickness and temperature distribution throughout the film. Biacetyl was used as a dopant, which emits phosphorescence as well as fluorescence when illuminated with UV-light. The fluorescence intensities in biacetyl, and most dopants, are temperature dependant which was isolated in order to make temperature measurements.

The laser light absorption technique is similar to the fluorescence method, but instead of involving the fluorescence of the film, the absorption of light passing through the film is used to determine film thickness. Unlike the fluorescence method, the laser light absorption technique requires two optical access points on the film which are

usually above and below the film. This limits the solid substrate to transparent materials only.

Wittig et al. [8] utilized this method for measuring the film thickness in an experimental test section designed to incorporate some of the characteristics of a prefilming airblast atomizer. The test section included interchangeable modules with windows for optical access, one of which was for a light absorption instrument. This instrument produced a laser beam that was split into four beams: two measuring beams, a reference beam, and a calibration beam. The reference and calibration beams were used to determine the fluid absorption coefficient. Methylene blue food coloring was used to color the fluid and because of the high absorption coefficients of this fluid, only a negligible mass flux was needed, which did not influence the film flow.

Barter et al. [9, 10] used a laser light absorption technique for simultaneous measurement of wave amplitude and surface angle. The experimental facility consisted of a container of water with a surface wave generator, where the mean liquid height was known. Thus, the experiment was not aimed at measuring the total height of the water, but only the amplitude of waves as compared to a known average water level. A green dye was added to the water to provide the measuring system with a detectable intensity.

Mouza et al. [11] validated film thickness measurements made using the laser light absorption method by making simultaneous thickness measurements using a "parallel wire conductance probe". The equipment used in the light absorption measuring system was listed in detail, including a 5 mW laser producing light at a wavelength of 635 nm, a silicon photodiode for light detection, an optical filter which allows only light with a 635 nm wavelength to pass, and a custom-made photodiode amplifier. The fluid

flow was carried through a loop with a transparent 24 mm inner diameter pipe for optical access. The working fluid was a solution of methylene blue dye dissolved in tap water in 25 ppm. The conductance probe was located a 10 cm axial distance from the light absorption measuring location. A comparison resulted in a satisfactory agreement between mean thickness data of the two measuring techniques. Limitations caused by the angle of the film surface and the response frequency of the photodiode are discussed. It was concluded that although light absorption measuring techniques have been mostly abandoned due to poor quality in light sources and detectors, advances in modern diode lasers and light detectors along with the miniaturizing of the electronics have rendered the technique an accurate tool.

Another laser technique involves internal light reflection from the liquid-gas interface due to the difference in refractive index of liquid and air. This method uses a light source on the outside of the film flow channel, which requires the film to travel through a transparent solid substrate. Light travels though the solid wall and is then transmitted through the film to the liquid-gas interface, where light is either reflected or transmitted depending on the light's incident angle. If the incident angle of light is equal to or greater than the critical angle for the given interface, then light will be reflected at the liquid-gas interface and will travel back through the film towards the solid wall. The internal light reflection technique utilizes this principle to reflect light onto the outside of the transparent wall, which creates an image that can be captured and processed to find the film thickness.

Hurlburt and Newell [12] utilized this technique for films in two-phase, annular flows. In this study, a thin coat of white paint was placed on the outside wall of the tube,

which served as a light diffuser. After transmitting through the wall and the film at various angles due to diffusion, any light that was internally reflected at the liquid-gas interface was projected back onto the outside wall of the tube. The experimental procedure involved a video camera to capture images of the light reflected onto the tube wall. Random individual frames were used to create bitmap files. These processed images showed a measurable distance from the point where light enters the tube wall and where light exits the tube wall. This distance is linearly proportional to film thickness. Mean film thickness measurements were made at three tube wall locations for five flow conditions. Film thicknesses ranging from 0.15 mm to 1.40 mm were measured, and standard error of mean film thickness for this technique was 4% to 10%.

Shedd and Newell [13] also applied the internal light reflection technique to films in two-phase annular flows in square and circular tubes. In this study, the light reflected onto the tube wall was captured by a charge coupled device (CCD) camera. It was discussed that if the reflected light reached the outside wall of the tube to be photographed by the camera, the light was traveling at an angle larger than the critical angle for the air-tube interface, causing total internal reflection within the tube wall. This situation is not desired and prevented the camera from receiving the reflected light, so a thin, frosted, plastic tape with a white adhesive was placed on the outside of the tube where film thickness was measured. This increased the critical angle of this interface, allowing light to transmit out of the tube wall to the camera. The image captured by the camera was processed by a computer program to determine the film thickness within 0.01 mm or better. In this study, film thicknesses ranging from 0.01 mm to a thickness equal to that of the tube wall could be measured. The process speed allowed approximately 2.5

thickness measurements per second. The accuracy of the technique was verified with a needle contact measurement method, and the average difference between these two methods was 2.2%. Mean film thickness results were presented for several locations on the tube wall for only one flow condition.

Samenfink et al. [14] presented an advanced film thickness measurement technique based on the absorption and deflection of laser light. This method involved an innovative optical receiving apparatus to measure the film thickness and film surface angle simultaneously. The significance of this method was rooted in the use of two laser beams traveling through the liquid film with different wavelengths. The first laser with λ_1=1480 nm was used for the actual film thickness measurements by absorption and the second laser with λ_2=830 nm was used in a correction scheme. The angle of the film surface was taken into account by the second beam because the lower wavelength of the second beam provided for almost zero absorption by the film. The intricate light receiving unit used an intensity detector for film thickness measurement, which used the light absorption technique as discussed earlier, and two position detectors were used for surface angle measurement. The thickness and angle measurements were used in conjuncture with a Laser Doppler Velocimeter (LDV), which allowed for velocity distribution information inside the film. The thickness/surface angle measuring system and the LDV system were synchronized by using the LDV system's timing as a triggering event for the thickness/surface angle measuring system. Used cooperatively, the results from these systems were used to make conclusions concerning the volume flux of liquid in the dynamic film.

Another method, known as laser interferometry, makes use of the phase shift between the reflection of incident light from the top and bottom surfaces of the film. This method only requires access to the liquid-gas interface of the film, which allows use with a number of different solid substrate materials.

Ohyama et al. [15] first developed the interferometry technique and constructed a prototype apparatus based on the principle. The beam from a 30 mW He-Ne laser was aimed at the film and reflected from both the top and bottom surfaces of the film. The reflected beams passed through a lens to form a parallel beam. This beam was projected onto a screen, forming an image of concentric circular interference fringes. A 35 mm camera was used to capture this image. The images were then used in conjuncture with geometric calculations using the spacing between fringes to determine film thickness. In this study, the films were assumed to be of approximately uniform thickness, on the order of 0.01 mm to 1 mm. The minimum measurable thickness was determined to be 0.01 mm for the apparatus used, but this minimum will depend on the wavelength of the laser light. Sources of error in this study included the human error involved in examining the interference fringes and a small error from the shift of light caused by the cover plate of the chamber holding the subject film.

Nosoko et al. [16] advanced the interferometry technique further. A significant change from the earlier work of Ohyama et al. [15] was that the laser beam was pointed at the film surface at an angle instead of perpendicular to the film surface. This method enabled the formation of interference fringes distributed more densely. Also, lenses with accurately defined focal length resulted in greater ease of interferometer setting and a higher accuracy in film thickness. No calibration was required for this technique. The

images were captured in the same method as [15]. The laser head, beam adjusting lenses, the screen, and the camera were mounted such that the assembly could be swung around the point of focus on the film, symmetrically about the normal to the film. The number density of fringes was adjusted by rotating this assembly, which allowed for an optimum number density of fringes to appear for a given film thickness. This study also discussed the application of the system to dynamic film thickness measurements. Dynamic films cause the fringes to change and sweep across the screen. This type of behavior can only be captured with a very high speed camera and bright lighting, neither of which was used in this study. Theoretical error calculations for this experimental setup depended on the angle at which the assembly was oriented with respect to the film. For laser beam angles in the range of 20°-70° with respect to the perpendicular it was estimated that the error should never exceed ±0.07%. Microscope cover glass was used to experimentally determine the error. Thickness measurements using interferometry were consistently 2% less than thickness measurements taken using a micrometer.

Kelly-Zion et al. [17] expanded the work of Nosoko et al. [16] to measure transient thickness of evaporating films. The noteworthy advancement of interferometric thickness measurement made in this study was the use of a high speed camera (Photron FastCam 1280 PCI) to capture fringe images. Previously, the imaging equipment was too slow to allow for transient film thickness measurements. Although flowing films were not measured, this study measured the film thickness of three volatile liquids: hexane, decane, and a mixture of both. The camera was used at framing rates ranging from 60 to 250 fps depending on the fluid measured. Increasing the frame rate had three main effects on the results. As the exposure time decreases for each image frame, more light is

potentially required. Secondly, more image samples require more memory storage capacity. Last, when the framing rate is very fast there must be a method of automating the image inspection process due to the high quantity of images. Kelly-Zion et al. [17] used a computer program written in Matlab to count the number of fringes in each recorded image with the aid of a Fast Fourier Transform (FFT). It is important to note that after time passed and the hexane film became small due to evaporation, the film surface angle at the laser reflection point became large, causing the reflected beam to steer away from the field of view of the camera. The film thickness total uncertainty for the measurements in this study was approximately ±11%. This was largely due to the uncertainty in the beam angles and the uncertainty in the fringe count.

Friedrich et al. [18] enhanced the technique described in [17] in order to measure average thickness of shear-driven liquid films. A significant change made for this application was the choice of angle of incidence, which must be adjusted properly in order to optimize the visibility of the interference pattern. Through preliminary testing, the angle of incidence providing optimum fringe visibility was found to be 30°. Past studies also used the angle of incidence to adjust the fringe density on the images. This technique though, used the receiving optics, not the angle of incidence, to change fringe density. The reflected fringe pattern was reflected onto a neutral density filter and the images were captured using a Photron 1280 PCI camera operating at 4000 fps, which was also chosen to optimize fringe visibility after preliminary testing. This interferometric technique had the ability to measure film surfaces up to 2° out of parallel with the bottom wall, which limited the data to the film thickness at peaks and valleys of waves only. But,

this information was used to determine the mean film thickness of the dynamic shear-driven films.

Laser Focus Displacement (LFD) technology has recently been used by a limited number of experimentalists to measure liquid film thickness. Within an LFD measuring unit, a laser source produces a diverging beam of light and the optical train within the unit utilizes the confocal principle to determine the location of an interface between two media. While moving the focal point of a converging laser beam, the LFD instrument locates a surface by sensing peaks in reflected light intensity when the laser's focal point is at the interface of two media. LFD instruments were first designed for detecting scratches in electrical devices, but a select few investigators have used the technology for dynamic liquid film measurements.

Takamasa and Kobayashi [19] were the first to use an LFD for liquid films. Their study applied the instrument to annular two phase flow of films inside a vertical tube. An LFD instrument manufactured by Keyence Co., Model LT-8100 was used, which provided spatial resolution of 0.2 μm and temporal resolution of 0.7 kHz. The LFD was mounted outside a vertical circular tube, and in order to measure films located on the inside of the tube the outside surface of the tube was made flat where at the LFD's location. Calculations including the refractive index of the transparent tube wall and the film were used to adjust the raw displacement data in order to account for the refraction of light at the air-tube interface and the tube-film interface. This calculation was checked in a preliminary test. The test used a tube cut in half and measurements adjusted with calculations were compared with measurements taken when the LFD was used on the open side of the film where light did not pass through the tube wall. This validation

resulted in a 1% margin of error. Another preliminary test was performed, utilizing the LFD to measure the tube vibrations caused by the system's pump. The oscillations were smaller than 5 μm. The experimental results compiled from measurements taken at several axial locations on the tube at several flow conditions offered valuable conclusions concerning wave formation. The thickness data provided by the LFD was used to calculate wave amplitude, wave frequency, maximum film thickness, minimum film thickness, and average film thickness. This study made an interesting comparison between the LFD measurements and measurements using a needle contact technique from another study. The maximum film thickness data agreed for each measuring technique, but the minimum film thickness was 0.2 mm using the needle contact technique and 0.1 mm using the LFD technique. This difference occurred because the needle contact point may cause error in minimum film thickness measurements due to the needle's presence disturbing the film.

Takamasa and Hazuku [20] conducted similar experiments used a laser focus displacement instrument to measure film thickness on a transparent vertical plate. A new concept introduced by [20] was the use of two LFDs simultaneously, with one placed on the film side of the vertical plate and one placed on the opposite side of the vertical plate. The laser beam focal points of each LFD were placed 1.5 mm apart to prevent the beams from interfering with one another. The film thickness results showed agreement between each instrument, with a slight difference due to the progressive motion of the film's waves. Using this difference, the wave velocity was calculated, which should not be confused with the film velocity.

Busam et al. [21] also utilized laser focus displacement technology for film thickness measurements in an aero-engine system where oil is used to lubricate bearings. A compact high speed bearing chamber served as a two phase flow generator for the investigations in a vent pipe section. The LFD was used to measure the mean thickness of oil film at two axial locations in upward annular flow. The influence of temperature, air mass flow rates, and fluid volumetric flow rates on the film thickness was observed for time averaged values. Busam et al. [21] also included a small conclusion concerning the film surface angle limitations of the LFD. It was noted that only waves with a maximum slope of about $\frac{\alpha}{2}$ between the surface and the optical axis of the sensor can be detected, where α is the cone angle of the incident laser beam.

Hazuku et al. [22] used an LFD paired with Particle Image Velocimetry (PIV) to perform an experimental study concerning the surface elevation of a free surface and liquid velocity profiles in pools of water. The main objective was to confirm the simultaneous measuring with LFD and PIV systems as a reliable technique. This was done by first confirming the accuracy of free surface elevations by measuring the free surface elevation with LFD and PIV systems simultaneously. Second, the spatial accuracy of the measuring system for three-dimensional surface inclination and particle positions was estimated using a small water tank in a preliminary test.

Hazuku and Fukamachi [23] made further verifications of the LFD technology by using an LFD to confirm the existence of extremely thin (~0.25 μm) liquid films on the inner tube surface in slug and annular flow regimes. It was confirmed that the thinnest measurable film thickness using an LFD was 0.25 μm. They also used an experimental test to determine the maximum measurable surface angle when glass is the subject piece.

In this test, an LFD was used to measure the location of the outside surface of a glass tube. If the LFD is centered on the tube, then the surface angle is zero degrees in relation to the laser beam axis, but if the LFD traverses across the tube then the surface angle increases in relation to the laser beam axis. The maximum measurable surface angle of the glass tube was 33°, which disagrees with the prediction of Busam et al. [21]. The inclination angle of the liquid film interface in annular flow was assumed to be smaller than 20°, thus allowing the LFD to detect the interface at all wave angles. These tests were performed with a Keyence Laser Focus Displacement Meter Model LT-8100.

Hazuku et al. [24, 25] have performed two more recent studies using an LFD to measure films in annular two phase flow. In [24] the mean film thickness was used to calculate a one-dimensional interfacial area concentration. A comparison was made between the interfacial area concentration from measured data and the interfacial area concentration calculated using a computational model for annular-mist flow. In [25] the LFD was applied to shear-driven annular flow in a vertical glass pipe 5mm in diameter. Recorded film thicknesses ranged from 100μm to 900μm, and mean film thickness and disturbance waves were studied. High speed imaging was used in conjuncture with the LFD's measurements, and the images showing large and small film thicknesses correlate well with LFD measurements taken simultaneously.

Each of the film thickness measurement techniques discussed above is accompanied by requirements that must be placed on the experimental system where the technique is applied. Some of these techniques constrain the experimental system's design with many requirements, while the more modern methods have small requirements that are less likely to invade the investigator's purpose. The most modern

method is the use of a laser focus displacement instrument. An LFD can be applied to any fluid type, unlike laser induced fluorescence, which requires the addition of a dopant. An LFD allows the use of opaque solid substrates, unlike light absorption or internal light reflection methods. Also, although an LFD cannot measure films with extremely large surface angles, the surface angle limitations are much smaller than that of interferometry. Finally, an LFD is a readily available as a complete system which requires little preliminary knowledge or training to operate. This gives the technology a great advantage over elaborate custom measuring systems that may match the LFD's capabilities, but require great efforts to construct and operate.

2.2. LIQUID FILM SEPARATION

While film thickness measurements have been performed by a multitude of investigators with a variety of techniques, a limited amount of work studies the behavior of these films at a sharp expanding corner. The motivation driving this work is primarily to gain the ability to predict the liquid behavior after the corner. As opposed to employing existing computational models, the goal is to derive an engineering model to describe flow in a time-averaged sense. This is significant in the case of shear-driven films, because of the dynamic instabilities in the film's surface structure, where instantaneous measurements and predictions are challenging. Applications where this behavior is important either desire the fluid to remain in a liquid phase and remain attached to the solid substrate or separate from the wall, break-up, and evaporate.

Hartley and Murgatroyd [26] made an early study that did not focus on the separation or break-up of a film at a sharp corner, but paid attention to the existence of dry patches in the flow of shear-driven and gravity-driven films. Their study focused only

on the conditions required to maintain dry patches after they are formed and not the initial formation of these dry patches. At the edge of a film adjacent to a dry patch the surface tension forces were balanced with the static pressure that is caused by the film velocity converging to zero at the edge of the film. It was determined that in order to sustain a wetted area on the solid substrate then the film must maintain a minimum film thickness. This minimum film thickness not only depended on the film velocity, surface tension, and density, but also on the contact angle formed at the edge of the film. The theoretical calculations were compared with experimental data from three other works. In two of these three comparisons the data agreed nicely, but there were large discrepancies in the third. It was projected that the disagreement may have been caused by a difference in experimental procedures, where starting at low film flow rates and increasing or starting at high film flow rates and decreasing could have a large effect on results. Particularly, contact angle could be influenced by these experimental procedure differences. Although the work of Hartley and Murgatroyd [26] did not address film separation at a corner, the methods used to address contact angle and forces from inertia, surface tension, and gravity can be applied to separation at a corner.

Owen and Ryley [27] used a radial stress model to determine the onset of film separation from a rounded corner. In the radial stress model film inertia, surface tension, and body forces are used to estimate the radial stress of a film traveling on a rounded corner. The film is attached to the rounded corner with a specific radius and film thickness and a positive radial stress in this case represents a compressive stress acting to keep the film attached to the wall. A negative stress is a tensile stress causing the film to separate from the wall. This stress balance is focused on a particle of fluid within the

film, and it is assumed that the stress at the surface of the film will be most positive, causing the film to completely separate from the solid surface when the stress at the surface of the film is zero. It is important to note that this analysis did not consider the formation of ligaments, which can greatly influence the treatment of surface tension forces and body forces. The formation of ligaments dictates an arm of fluid that has detached from the solid surface but remains attached to the original film. The radial stress model assumes that once the film detaches from the solid surface then complete separation has occurred, with no ligament formation. This model will be discussed further with detailed comparisons in the film separation experimental results section.

Investigation by James et al. [28] concentrated on liquid re-entrainment in wave-plate mist eliminators, where the primary gas flow travels through a series of sharp bends causing droplets to collide with the channel walls. The main interest here is to cause entrained droplets to attach to the wall and drain away from the gas flow, thus eliminating mist from the gas flow. When droplets attach to the wall a liquid film is created, and if the film separates from the wall upon reaching the wave plate corners then liquid re-entrains into the gas flow. This re-entrainment prevents the liquid from being removed from the system. Thus, film separation is undesired in this application. This study investigated the causes of film separation by measuring film separation in a wave-plate mist eliminator operated at a range of flow conditions. The effects of system parameters such as corner angle, gas phase velocity, and liquid loading within the gas phase were considered in order to create a model to predict whether or not re-entrainment takes place.

A more common application motivating film separation investigation is the intake system of a port fuel injection engine. O'Rourke and Amsden [29] and Maroteaux et al. [30] have studied liquid films in intake ports during engine cold start. The question addressed here is whether or not the liquid fuel will remain attached to solid surfaces, which are below boiling temperatures during cold start conditions, or re-entrain into the intake gas flow to form a well atomized fuel-air mixture. Correct prediction of these cold start film behaviors will improve fuel-air mixtures and lower unburned hydrocarbon emissions. Computational models developed in the work of O'Rourke et al. [29] and Maroteaux et al. [30] provided better methods for these applications.

O'Rourke and Amsden [29] developed a model for predicting break-up of a liquid film in a port injected spark ignition engine. This model encompassed the entire process of film break-up from a thin liquid film in an intake port to a vaporized fuel entering the engine. This computational process included a separation criterion specifically for separation from a solid wall at a sharp corner. As the film approached a sharp corner then the liquid inertia worked against the low pressure region that forms on the wall side of the film. Film separation was based on the pressure difference between the pressure on the gas side, which is the gas pressure, and the pressure on the wall side. This pressure difference, according to [29], causes the film to turn and remain attached to the wall unless the liquid inertia is large enough to overcome the pressure difference. This study made notable assumptions based on the existence of thin liquid films. With film thicknesses less than 100 μm, it was assumed that wall film inertial terms are negligible, pressure gradient terms are negligible, gravitational forces are negligible, changes in the film velocity due to vaporization are negligible, and the velocity profile in the film varies

linearly with distance from the wall. Included in the linear velocity profile assumption is the assumption that all liquid velocities in the film are tangent to the wall. It is also important to note the events occurring at the point of separation. In this model, when the separation criterion is satisfied, the liquid film is converted to spray droplets at the corner. The contributing TAB droplet break-up model causes the droplets to break-up into small, aerodynamically stable sizes very quickly due to large gas phase velocities. At separation, it is assumed that the initial droplets are traveling at a velocity equal to the film velocity and are sized at a radii half of the value of the film thickness. Due to the utilization of the TAB break-up model though, the initial size and velocity of the droplets is not significant because the break-up causes these values to assimilate rapidly to the gas phase velocity. The important overlying assumption to note though is that the films did not form ligaments in the model and have negligible gravitational forces during separation due to small droplet sizes.

Maroteaux et al. [30] constructed a model for fuel film separation and atomization near the sharp edges of the intake system of a port fuel injection engine. This study distinguished two categories of disturbances that develop at liquid-gas interfaces and cause film break-up. These are aerodynamic instabilities caused by the shearing effect of air flowing at high velocities adjacent to the film, which induces liquid stripping at the interface (i.e., Kelvin-Helmoltz instabilities), and gravitational or inertial instabilities occurring when two adjacent fluids are subject to a body force (i.e., Rayleigh-Taylor instabilities). The former was used to predict the atomization of fuel films from port walls and intake valve surfaces. The latter, inertial or gravitational instabilities, was used to create a computational model for film separation, which is of interest here. The criterion

used for the separation model was based on a ratio between the final amplitude of a wave disturbance and the initial amplitude. This disturbance amplitude ratio was given a critical value by using experimental data from the same study, where a ratio greater than the critical ratio will result in film separation. Below this value, stripping is never or sporadically observed. Even at disturbance amplitude ratios above the critical ratio though, the experimental results still showed a certain part of the film that flows around the corner and does not separate. From experimental visualization, the critical disturbance amplitude ratio was given a value of 20. From this point, the film velocity, film thickness, wave growth rate, and the corner angle were used to determine a critical corner angle for a particular film velocity and thickness. Many assumptions within this strategy were criticized by Gubaidullin [31]. First, a criticism of the wave growth calculation noted that when calculating the acceleration term used within the wave growth term using the methods of Maroteaux et al. [30]. The acceleration calculation resulted in extremely large, unrealistic numbers when applying the film thicknesses and velocities used in [30]. Second, the resulting wave growth calculations also result in unrealistic numbers. Third, the use of one corner angle in the experimental system is inappropriate for making conclusions about the film separation criterion since the theoretical predictions are based on these experimental results. Finally, it was criticized that only one fluid, dodecance, was used in the experimental study and in order to establish a reliable correlation experimental data for fluids with various physical properties should be obtained. Such comments made by [31] reminded that there is a wide range of factors to consider when studying film separation.

Carvalho and Heitor [32] considered the break-up of films in prefilming airblast nozzles in their work. Although the geometry of the liquid film in an airblast nozzle consists of an annular shape, much of the same conclusions from prefilming airblast nozzles concerning break-up are related to flat liquid sheets and films. An experimental apparatus was developed to mimic this application, and Reynolds numbers ranging from 6600 to 66000 and 27300 to 92900 for the inner and outer air flows, respectively, allowed for a wide range of flow conditions. Ligament break-up length was a primary parameter of consideration. Increasing inner or outer gas phase velocities, or both, resulted in shorter break-up lengths, while increasing film thickness or film velocity resulted in longer break-up lengths. A significant conclusion of this study was the existence of ligaments at the circular jet corner, and these ligaments had characteristic lengths with a heavy dependence on gas phase velocity.

An experimental study of ligaments formed by liquid sheets was performed by Arai and Hashimoto [33], resulting in an empirical equation to determine a characteristic ligament length for a given set of parameters. Ligament length was shown to be a function of the liquid Reynolds number, a relative Weber number relating the gas phase and liquid phase velocities, and the liquid thickness.

Steinhaus et al. [34] made an experimental apparatus to measure film separation and compared the results with the model proposed by Maroteaux et al. [30]. This experimental apparatus did not only allow for visualization of the separation, but measured the mass of liquid which remained attached after the corner by removal through a drain with suction. The results showed significant disagreement with the computations from [30]. This was shown by calculating a critical corner angle of ~80˚ using the method

proposed in [30] for the highest experimental flow rates. At these high flow rates, the experiment resulted in high amounts of film separation for a corner angle of 45˚. Thus, the proposed critical angle of 80˚ is in disagreement because the critical angle suggests a threshold where smaller angles will result in little or no separation.

Friedrich et al. [35] also constructed an experimental apparatus to measure the amount of film separation at a sharp corner. Their study proposed a film separation criterion using force balance and then verified this theoretical method using experimental results. The experimental facility constructed was similar to that of Steinhaus et al. [34], but an important difference existed in the method of removing the liquid that remained attached after negotiating the corner. In the experimental apparatus of Steinhaus et al. [34] the liquid that does not separate was removed through a drain located a significant distance downstream of the corner, whereas Friedrich et al. [35] used a drain located a short distance, 5 mm, after the corner. In the latter situation film was removed immediately after the corner, which prevented the drain from removing liquid that separated at the corner and then fell downward to land on the bottom wall. The theoretical portion of Friedrich et al. [35] proposed a force ratio to determine the onset of film separation. The force ratio was calculated using forces of inertia, gravity, and surface tension in order to compare forces causing separation with forces preventing separation. The onset of separation was predicted to occur at a force ratio equal to one, and experimental data agreed with this projection. This technique paid attention to the physics of ligaments during the film separation process because the existence of ligaments at the corner was confirmed by high speed imaging. The addition of ligament behavior into the film separation criterion added previously nonexistent surface tension forces and greatly

affected the gravitational force calculation. The force ratio used the empirical equation developed by [33] to calculate a ligament length to determine the actual size, and thus the mass, of ligaments at the point of separation.

Over time, researchers have come to accept that a multitude of factors must be included in film separation physics, especially when dealing with shear-driven films as in the current study. These factors mainly include gas phase velocity, film thickness and velocity, corner angle, wave disturbances, ligament behavior, and the fluid properties of density, viscosity, and surface tension. All of the studies mentioned above have neglected to address at least one, if not many, of these factors. Applications such as port fuel injected engines will benefit greatly from a film separation model that can be applied to the wide range of relevant fluids and flow conditions, but until investigators include all of these factors in their studies, computational models must use unreliable assumptions when involving films flowing over sharp corners.

The work presented here seeks to produce valuable film separation data from reliable experimental methods, which will provide a validation point for current separation models. But, separation models use the flow conditions immediately before the corner as initial conditions, which means that in order to compare this study's experimental separation data with other models, flow conditions just before the corner must also be determined for each flow condition. Computational models can fill this need by predicting the film's velocity and thickness for given flow conditions, and this is how Friedrich at al. [35] predicted the average film velocity and thickness at the corner. Friedrich et al. [35] used a two-dimensional film propagation computer simulation to estimate these two parameters. Then, the force ratio predicted the onset of film separation

using these estimations. Thus, the force ratio validation relied on the accuracy of the film propagation model.

This study improves the work of [35] by making experimental measurements, not computations, to determine the initial conditions for force ratio calculations. Film thickness measurements at a location just upstream from the corner will accompany film separation data in order to associate a measured amount of separation with actual film conditions at the corner. The force ratio will be calculated for each flow condition by using measured average film thickness data and average film velocity values calculated using thickness data and the known volumetric film flow rate. Since there are numerous film thickness measurement techniques, the method chosen for this study will be validated as a suitable shear-driven film thickness measurement technique. The chosen experimental methods will be described in detail, and both separation and thickness measurements will be compared to theoretical models. Also, this study will investigate the effects of viscosity on the film separation process, whereas [35] investigated the effects of surface tension only. This study employs a better test matrix by using three different fluids in order to isolate the effects of both surface tension and viscosity.

3. QUALIFICATION OF A LASER FOCUS DISPLACEMENT INSTRUMENT

3.1. INTRODUCTION

A laser focus displacement instrument utilizes the confocal principle with laser light to determine the location of an interface between two media. By moving the focal point of a converging laser beam, the LFD instrument locates a surface by sensing peaks in reflected light intensity when the laser's focal point is at the interface of two media. This technology is most widely utilized in product testing and product quality verification that requires fine surface finishes or material thickness. Originally developed for detecting scratches on electrical devices, the LFD is also used in applications such as measuring the surface profile of a brake disc, measuring glass thickness, and measuring the thickness of a contact lens in the plastic industry.

Within the LFD measuring unit, a semiconductor laser source produces an unpolarized, diverging beam of light as shown in the diagram in Figure 3.1. A collimating lens then precedes an objective lens, which causes the beam to converge to a point at a known location. The focal point is moved up and down by moving the objective lens in an oscillating manner. This is achieved by constraining the collimating lens to a known location and securing the objective lens on one of the vibrating prongs of a tuning fork. The tuning fork is then subject to a known frequency from a vibration source and in turn, the objective lens oscillates at a known frequency and amplitude. The focal point of the beam scans up and down at the same frequency and amplitude as the objective lens. When the focal point is located on the target surface, then the light will be reflected back into the LFD measuring unit with greatest intensity. When light passes through the pinhole shown in Figure 3.1, the light receiving element senses a light

intensity peak. With a known location of the oscillating objective lens measured by a position detection sensor, the LFD can match the light intensity peak with a focal point location. Thus, the target surface location can be determined.

Figure 3.1. Laser focus displacement measuring unit diagram.

This study examines the abilities of the LFD technology as a fluid dynamics tool. Fluids experimentation offers the technology a measuring environment more demanding than the conventional applications of LFD technology. Liquid film thickness measurements can be performed with a LFD instrument as shown by recent studies ([19-

21, 23-25]), but when such measuring is performed with rapidly changing film thicknesses and steep surface angles, the limitations of the device are noticeable. These limitations must be defined and the operations of the measuring unit must be understood in order to successfully utilize this technology for dynamic liquid film thickness measurements.

3.2. THICKNESS LIMITATIONS

Limitations on the thickness of the subject piece are determined by the oscillation range of the objective lens. Any surfaces that lie outside of the range of the focal point cannot be measured. If the thickness of an object is to be measured, for example, the top of the subject must be below the maximum height of the focal point and the bottom surface must be above the minimum height of the focal point. When these constraints are met, the LFD instrument can measure the location of two surfaces.

It should be noted that in applications where film thickness measurements are needed but the film thickness, h, is greater than the oscillating range of the focal point then thickness measurements are still possible. These situations simply require the measuring unit to be placed such that the distance from the mean focal point location and the solid substrate is known. When the oscillating range of the objective lens is greater than the subject thickness, displacement data for the top surface and bottom surface of the subject can be output within the cycle of the objective lens oscillation, allowing for thickness measurements. The light reflected off the top surface is not influenced by the material of the subject piece, but when measuring the location of the bottom surface the material's refractive index must be used to make corrective calculations due to the

refraction of light passing through the material to reach the bottom surface. This calculation must include the surface angle of the top surface of the subject and the refractive index of the subject material. Two additional properties must be included which are depicted by the laser focus displacement instrument being used. First, the divergence angle of the beam and second, the wavelength of the laser light is needed in order to determine the refractive index of the subject. Thickness, h, can then be calculated as

$$h = h' \frac{\sin\alpha + (\cos\alpha)\left[\tan\left(\frac{\theta_c}{2} - \alpha\right)\right]}{\tan\left[\sin^{-1}\left[\frac{n_{air}}{n}\sin\alpha\right]\right] + \tan\left[\sin^{-1}\left[\frac{n_{air}}{n}\sin\left(\frac{\theta_c}{2} - \alpha\right)\right]\right]} \quad (1)$$

where h' is the difference between the measured locations of the top and bottom surface, n_{air} is the refractive index of air, n is the refractive index of the subject material, α is the angle of the top surface of the subject, and θ_c is the exit cone angle of the beam. The derivation of (1) is found in Appendix A.

3.3. SURFACE ANGLE LIMITATIONS

The LFD technology is also limited by the surface angle of the subject. The surface angle must be small in order for the light receiving element to detect a light intensity peak. Large surface angles cause the light to scatter when reflected instead of reflect back into the measuring unit to be detected by the light receiving element. The maximum possible surface angle has been experimentally predicted by Hazuku et al. [25]

by measuring a glass column with a diameter of 5mm using a Keyence Model LT-8100 Laser Focus Displacement Instrument. The maximum surface angle allowing detection was 33° in this study. Theoretical predictions by Busam et al. [21] were made based on the cone angle of the optics, where the maximum angle was approximated as α/2 with α as the laser beam cone angle.

To investigate the angle limitations of the LFD instrument the measurability of the top and bottom surface were investigated theoretically and experimentally. In the case of both top and bottom surface measurements, the subject material and the surface angle will influence the amount of light that is reflected or refracted at the interface. As a result, theoretical calculations proceed by investigating surface angle influences and subject material influences. These calculations will proceed by making geometric calculations for top surface reflection followed by bottom surface reflection. Then, material reflectivity influences will be introduced as an important factor in surface measurability

3.3.1. Top Surface Calculations. First, calculations predicting the maximum surface angle for measuring the location of the top surface were made. Figure 3.2 shows the path of light resulting from top surface reflection, where the surface angle, α, is measured from the horizontal. Previous theoretical predictions of the maximum angle for detection made by Busam et al. [21] compared the surface angle to the laser cone angle, θ_c. Similar comparisons were made in more detail for this study. The projection of the reflected laser on the objective lens forms a circle and as α changes, so does the location and shape of this projected area. As α deviates from zero, the reflected laser cone projects an ellipse shape on the objective lens. The center of the projected ellipse moves farther away from the original center of the laser beam as α increases, resulting in a projected

area represented in Figure 3.3(a). As α increases, the amount of light reflected back through the objective lens decreases and it becomes more difficult for the LFD's light sensing element to detect the light intensity peaks needed to measure the target surface. It is important to note that for simplicity it is assumed that for light to be detected by the light receiving element the path of reflected light must overlap the original path of the incident light. Therefore, the aperture size of the light receiving element is not used in this study.

(a) (b)

Figure 3.2. (a) Path of incident laser beam. (b) Path of reflected laser beam.

Calculations were performed to study the amount of light reflected over the original path of incident light. Using integral calculus for the functions of a circle and an ellipse, the area of the intersecting region A in Figure 3.3(a) was calculated as a function of α and related to $A(0°)$, where $A(0°)=\pi R^2$. R is the radius of the circle shown in Figure 3.3(a). Figure 3.4 shows $A(\alpha)/A(0°)$ plotted versus α/θ_c, which presents large changes in $A(\alpha)/A(0°)$ as α/θ_c deviates from zero. Also, due to the design of the semiconductor laser

Figure 3.3(a). Projected area of light due to top surface reflection as viewed from above the objective lens.

Figure 3.3(b). Projected area of light due to bottom surface reflection as viewed from above the objective lens.

source there is a higher light intensity at the center of the laser beam than at the outside edges of the laser beam. This concept should be considered by studying the location of the center of the laser path. Calculations were performed to determine the location of the center of the laser path, x_o, as a function of α. These parameters, x_o and α, were

Figure 3.4. Relative area of the reflected light from top surface reflection plotted versus surface angle.

Figure 3.5. The reflected laser center location plotted versus the subject surface angle, normalized by the incident cone radius and the cone angle, respectively. (top surface reflection)

normalized with relation to the cone radius R and the cone angle θ_c, respectively. R and θ_c are constants. Figure 3.5 shows x_o/R as a function of α/θ_c. When x_o/R=1 the center of the reflected laser path has reached the outside edge of the incident laser path. This situation occurs when α/θ_c=0.5. As a result, when x_o/R approaches 1 then large amounts of light are lost due to reflection, because the greatest light intensities are located near the center of the laser beam.

3.3.2. Bottom Surface Calculations. To investigate the angle limitations for the measurability of the bottom surface, further theoretical calculations were performed. To appropriately address the case of liquid film measurements where the top surface is an air-fluid interface and the bottom surface is a fluid-solid interface, calculations were performed with a variable top surface angle and a constant bottom surface angle of 0°. This addresses cases where a liquid film flows over a solid substrate which has a flat surface perpendicular to the path of the laser.

Figure 3.6. Bottom surface reflection diagram.

This situation is represented in Figure 3.6, which shows the refraction of light at the air-fluid interface. Note that as α increases the reflected light is projected further to the left, whereas in Figure 3.2 the opposite trend is shown. Theoretical predictions of the maximum top surface angle for measuring the bottom surface required knowledge of the measuring unit geometry, subject thickness, and the subject material's refractive index. These calculations are similar to those performed for top surface predictions, but must account for the refraction of light passing through the subject material. Once again, the amount of laser light reflected over the original path of incident light is of interest because it is assumed that for light to be captured by the light receiving element the laser must be reflected over the incident laser path. Similar to the methods described above, the area of the intersecting region A in Figure 3.3(b) was calculated as a function of α, where Figure 3.3(b) shows the projection of the reflected beam at α>0° (ellipse), and the projection of the reflected beam at α=0° (circle). R is the radius of the circle shown in Figure 3.3(b). Similar to Figure 3.4, Figure 3.7 shows $A(\alpha)/A(0°)$ versus α/θ_c. Figures 3.4 and 3.7 depict similar trends, but Figure 3.7 includes $A(\alpha)/A(0°)$ values for three different refractive indexes in order to show the influence material has on refraction geometry. When water is used the reflected laser's projected area overlapping onto the path of incident light is almost equal when comparing bottom surface reflection to top surface reflection. Figure 3.7 also shows that refractive index has a significant effect on the area of reflected light. A subject material with a large refractive index will cause surface angle to have a greater influence on the amount of reflected light. The influence of subject thickness on bottom surface reflection was also investigated. For all three refractive index values shown in Figure 3.7, $A(\alpha)/A(0°)$ was calculated for thicknesses of 0.5mm, 1.0mm,

Figure 3.7. The relative area of the reflected light from bottom surface reflection plotted versus surface angle.

and 2.0mm. This range of values represents common thicknesses for dynamic film studies [8, 12], and changes in $A(\alpha)/A(0°)$ within this range were negligible. Thus, thickness variation was not given further consideration for this study. Proceeding in the same manner as before, calculations were performed to determine the location of the center of the reflected laser path, x_o, as a function of α. Figure 3.8 shows x_o/R as a function of α/θ_c, for three refractive indexes. For water (n=1.333), at α/θ_c=0.3 the center of the reflected laser path is now at the edge of the incident laser path, thus x_o/R=1. As α approaches α/θ_c=0.3 large amounts of light intensity will be lost due to the center of the beam path containing the greatest light intensities. Understanding the physics of the reflected laser beam, either the projected area, $A(\alpha)$, or the location of the intense beam

Figure 3.8. The reflected laser center location plotted versus the subject surface angle, normalized by the incident cone radius and the cone angle, respectively. (bottom surface reflection)

center, x_o, can provide insight as to the amount of light received by the light receiving element. But, when viewing these quantities individually any conclusions about the received light will be vague.

3.3.3. Relative Power Calculations. Judging relative areas or beam center locations will only give geometric values, but these calculations can be used to establish a more useful parameter, which is P/P_o, a ratio of the total power of light received by the LFD, P, and the total power of incident light, P_o. The total power (or flux) of a beam of light is a product of the cross sectional area of the beam and the mean intensity of light throughout the beam, or the electric flux density per unit time [36]. Thus, P will be determined by the area of reflected light, $A(\alpha)$, and the intensity of light, I, which is

variable throughout the laser beam. Since the intensity profile of the beam is unknown, values for P cannot be calculated, but an approximation of the P/P_o ratio can offer an estimate of how much of the incident light's power is received by the LFD. The recently discussed geometric calculations will provide an excellent starting point for predicting P/P_o as a function of α/θ_c.

There are three important points that can be drawn from the $A(\alpha)$ and x_o calculations. First, the point at which $P/P_o=1$ occurs when $\alpha=0°$, allowing all of the reflected light to retrace the path of incident light. Second, $P/P_o=0$ when $A(\alpha)=0$, which is known from the previous calculations. For example, Figure 3.4 shows that $A(\alpha)/A(0)=0$ when $\alpha/\theta_c=1.12$. Thus, $P/P_o=0$ at $\alpha/\theta_c=1.12$. Third, $P/P_o\approx0.5$ when the center of the reflected beam is located at the edge of the incident beam path, when $x_o/R=1$. For example, Figure 3.5 shows that the center of the beam path is located at the edge of the incident beam path when $\alpha/\theta_c=0.5$. These three points ($P/P_o=1$, $P/P_o=0$, $P/P_o\approx0.5$) are enough to create an estimated plot of P/P_o versus α/θ_c when another assumption is added concerning the slope of P/P_o at these points. As α increases, when the center of the reflected beam path is crossing the edge of the incident beam the P/P_o value is expected to decrease drastically due to the majority of the beam's power being concentrated in the center of the beam. With this conclusion, it was assumed that $\frac{d\frac{P}{P_o}}{d\frac{\alpha}{\theta_c}}=-\infty$ at $x_o/R=1$ and

Figure 3.9. The relative power plotted versus the subject surface angle divided by laser cone angle. (top surface reflection)

Figure 3.10. The relative power for 3 refractive index values plotted versus the subject surface angle divided by laser cone angle. (bottom surface reflection)

P/P_o=0.5. Using this concept, the known (P/P_o, α/θ_c) points are interpolated which gives a plot such as the result shown in Figure 3.9, which is the case of top surface reflection. Figure 3.10 represents the same situations as previously presented in Figures 3.7 and 3.8, but is a result of the P/P_o versus α/θ_c plotting method described above. This relative power-surface angle relationship is a much better representation of the energy received by the light receiving element and the important trends formed at particular surface angles. Comparing Figure 3.7 with Figure 3.10 reveals the importance of accounting for the location of the center of the reflected laser beam. Figure 3.10 shows that for water (n=1.333) at α/θ_c=0.5 the light reflected back into the LFD constitutes only 18% of the incident light even though $A(\alpha)/A(0)\approx 0.5$. Although the calculated relative power is a valuable expression of the modes by which surface angle influences light reflection, the subject material must be investigated to provide further details. At this point in this study, material effects have only been assessed in terms of the way refraction angles are affected, but now material effects will be investigated in terms of the reflection coefficient.

3.3.4. Reflectivity. A material that inherently reflects more light than other materials is expected to allow for higher limitations in surface angle, and in order to analyze this further, the reflection coefficient was calculated for different materials at various surface angles. The reflection coefficient is dependent on the refractive index of the material, n, and the incident angle of light, θ_1, and is used to determine the amount of reflected light intensity by the equation

$$I_r=\rho I_o\,, \tag{2}$$

where ρ is the reflection coefficient, I_o is the incident light intensity, and I_r is the reflected light intensity. This situation is shown in Figure 3.11, where part of the incident light is reflected at an angle θ_r and part of the incident light transmits through the interface and is refracted at an angle θ_2. In this application, reflection is assumed to be specular, meaning that $\theta_1=\theta_r$. To calculate ρ for a situation such as that shown in Figure 3.11 where an interface exists between two media with known refractive indexes, n_1 and n_2, and a known θ_1, the Fresnel equations follow as

$$\rho_{\perp} = -\frac{\sin(\theta_1 - \theta_2)}{\sin(\theta_1 + \theta_2)} \tag{3}$$

$$\rho_{//} = \frac{\tan(\theta_1 - \theta_2)}{\tan(\theta_1 + \theta_2)} \ . \tag{4}$$

For unpolarized light

$$\rho = \frac{\rho_{\perp} + \rho_{//}}{2} \tag{5}$$

where $\rho_{\perp}$ is the reflection coefficient for light polarized with the electric field of the light perpendicular to the plane of Figure 3.11, and $\rho_{//}$ is the reflection coefficient for light polarized with the electric field of the light parallel to the plane of Figure 3.11. Using the Fresnel equations for unpolarized light, the reflective coefficient was calculated for a

Figure 3.11. Light reflection and refraction at the interface of two media. ($n_2 > n_1$)

range of incident angles, and it was determined that for a change in the incident angle from 0° to 10° the reflection coefficient increased by 0.05% for water in air (n_w=1.333), 0.04% for optical crown glass in air (n_o=1.5198), and 0.03% for sapphire in air (n_s=1.7644). For electrically conductive materials, such as aluminum, the refractive index contains an imaginary part, k, where

$$m = n(1 - ik) \ . \tag{6}$$

For example, when Snell's Law is applied to the case of light crossing the interface of a dielectric medium and a conductive medium the imaginary component of the refractive index causes Snell's Law to follow as

$$n_1 \sin\theta_1 = m_2 \sin\theta_2 = n_2(1 - ik_2)\sin\theta_2 \tag{7}$$

where n_1 is the refractive index of the dielectric medium and m_2 includes the real refractive index of the conductive medium, n_2, and the imaginary part, k_2. A different form of the Fresnel equations must be utilized to include the imaginary part of a material's refractive index [37]. Proceeding with n_a=1.44 and k_a=3.694 for aluminum, the Fresnel equations show a 0.002% change in the reflection coefficient for aluminum in water when incident angle changes from 0° to 10°. By making these calculations for various materials, it was concluded that the change in the amount of reflected light intensity due to a change in surface angle is negligible. But, when isolating the refractive index influences by changing the material while maintaining a constant angle of incidence the changes are notable. At θ_1=0° the reflection coefficient of water, optical crown glass, and sapphire in air is 0.0205, 0.0424, and 0.0762, respectively. The reflection coefficient of aluminum in water is 0.7870. Such changes in ρ were used within the theoretical predictions of surface angle limitations, because it is expected to observe increasing surface angle limitations with an increasing reflection coefficient.

Using the preceding concepts regarding the reflection coefficient, the relative power, P/P_o, was adjusted to include reflection coefficients for the air-water interface and the water-aluminum interface below the film. For top surface measurements of water the

P/P_o values shown by Figure 3.9 were multiplied by ρ_w to give the result shown by Figure 3.12. Due to the small reflection coefficient of a water-air interface (ρ_w=0.0205), Figure 3.12 shows a significant effect from including the reflection properties of the interface. In the case of bottom surface reflection, the larger reflection coefficient for the aluminum-water interface will have a less significant effect on P/P_o. Examining the physics described by the Fresnel equations shows that 78.7% of light is reflected at the water-aluminum interface. When making bottom surface measurements though, light must travel from the LFD instrument through the air-water interface, reflect off the water-aluminum interface, and then travel through the water-air interface to reach the LFD. Therefore, the retained light intensity decreases at each of these three interfaces. Using this concept, calculations showed 75.6% of the original light intensity is retained when measuring the water-aluminum interface beneath a film. Since the amount of light lost due to absorption is negligible, it was assumed that a reflection coefficient of 0.756 should be multiplied by P/P_o to include the reflection properties of the interfaces. Figure 3.13 shows material reflectivity effects on a bottom surface reflection situation where $\rho_{al/w}$=0.756.

In order to use these relations for predicting the maximum surface angle allowing measurements, a minimum relative power value is needed. A baseline number can provide a threshold representing the minimum amount of incident light needed for the LFD to detect an interface. If this threshold is known then the maximum surface angle allowing measurements can be determined by finding α/θ_c at the point where relative power is equal to the threshold value. To establish this threshold, or minimum relative

Figure 3.12. The relative power with and without including the reflection coefficient plotted versus the subject surface angle divided by laser cone angle. (top surface reflection)

Figure 3.13. The relative power with and without including the reflection coefficient plotted versus the subject surface angle divided by laser cone angle. (bottom surface reflection)

power, experiments were conducted to find the maximum surface angle allowing measurements in a static, controlled situation. The maximum angle determined from these experiments was used in conjuncture with the previously discussed $\rho(P/P_o)$ versus α/θ_c calculations in order to find the minimum relative power. Next, this study will proceed by explaining the performed experiments and their results, including the prediction of a minimum relative power.

3.3.5. Static Liquid Displacement Measurements.

3.3.5.1. Measurement technique. In this study, a Keyence laser focus displacement instrument, model LT-9030, was used. Measurement range, which is the total vertical movement of the focal point, is 2.0mm for the LT-9030. The spatial resolution is 0.1μm and the spot diameter of the focal point of the laser is 7μm. The cone angle, θ_c, is 23°. The sampling frequency of the LFD is 1.5625 kHz, which corresponds to a cycle time of 0.640 ms. This speed is not fully realized in data collection due to the reset time of the LFD controller, which is 3 times the raw cycle time. Including the reset time results in a cycle time of 1.92 ms and a frequency of 520.83 Hz.

Displacement measurements were made for a static liquid bubble. 50μL of a water-surfactant mixture was placed on a flat polished aluminum plate creating a liquid bubble as shown by the image in Figure 3.14. The aluminum surface is secured at 0˚ from the horizontal with an uncertainty of ±0.5˚. The surface angle of this bubble relative to the horizontal is largest at the outside edges of the fluid and smallest at the apex in the center, which results in areas near the perimeter of the bubble where the surface angle is too large for measuring. In making such measurements, the laser focal point traveled from the edge towards the center of the fluid and then continued towards the opposite

edge of the fluid. The first data point was recorded at the first measurable location. The last data point was recorded at the last measurable location.

Figure 3.14. 50μL of a 0.1% surfactant mixture placed on a polished aluminum surface.

Image analysis was used to find the surface angle at the limits of measurement. A photo of each liquid bubble was analyzed using the image analysis features of Matlab. This involved a step by step procedure for each image in order to use the raw image to create a polynomial function representing the surface profile of the liquid bubble. First, Matlab used the image in bitmap format to create a black and white image including shades of gray, where each pixel within the image has a value ranging from zero to one. Zero represents a white pixel and one represents a black pixel. This grayscale image was used to create a black and white image eliminating all shades of gray. To make this

purely black and white image, a predetermined pixel value was used as a threshold for categorizing all gray pixels as either black or white. The result is an image with all pixels having a value of zero or one. The pixel value threshold was chosen such that all pixels within the liquid portion of the image become black, and all pixels within the air portion of the image become white. Within a looping computer code the pixels were analyzed to determine the location of the liquid-air interface by outputting the pixel location of the interface, and this computer code can be found in Appendix A. For all repetitions of this process one pixel represents approximately 60μm, which results in an uncertainty of ±30μm when converting spatial units from image pixels to microns. A plotting program used the computer code output in order to create a surface profile of the liquid bubble. A sixth order polynomial equation was fitted to this profile, and by finding the derivative of the fitted equation, the surface angle was determined for all locations. During the time passed during the measuring process, the liquid bubble partially evaporated which changed the height of the bubble without changing the location of the edge of the bubble. To address this, photos were taken immediately before and after the measuring process which provided one image for left side calculations and one photo for right side calculations, where the bubble has decreased in size during the measurement process.

In order to experimentally validate the maximum surface angle for measuring the bottom surface, the same 50μL liquid bubble method was used for displacement measurements. Similar to the previously mentioned top surface measurements, displacement data for the aluminum-water interface was attained where the interface was detected by the measuring unit. Although the target surface was the aluminum-water interface which was oriented such that $\alpha = 0°$, if the water-air surface angle was very

large then the flat aluminum-water interface was not measurable. This situation arises when the light passing through the water-air interface is refracted at a large angle, causing the light that reflects off the target surface to scatter away from the measuring unit instead of reflect back into the light sensing element. Thus, as was the case for measuring the water-air interface, there is a small area near the perimeter of the bubble where the target surface was not detected due to the large angle of the water-air interface.

3.3.5.2. Results. The results from this method are presented in Figures 3.15 and 3.16, where 0.1% and 1.0% surfactant samples are shown, respectively. In finding the maximum angle allowing detection, the derivative of the fitted polynomial equation was used for the first and last data points. For example, the calculated results for the 0.1% surfactant sample in Figure 3.15 are α=6.23° at the left limit of the profile and α=6.28° at the right limit of the profile. This procedure was repeated for both the 0.1% and 1.0% surfactant samples. The mean maximum angle allowing detection was 6.38° for 0.1% mixtures and 5.47° for 1.0% surfactant mixtures.

Due to the ability of the LT-9030 model to measure two surfaces within each oscillation cycle of the objective lens, the displacement data shown in Figure 3.15 is for the same liquid bubble as that which is shown in Figure 3.17. Figure 3.17 includes displacement data of the bottom surface instead of the top surface. The data shown in Figure 3.18 corresponds to the liquid bubble shown in Figure 3.16. In finding the maximum angle allowing detection, the derivative of the fitted polynomial equation was used for the first and last data points, consistent with the method described in the previous paragraph. For example, the calculated results for the 0.1% surfactant sample in Figure 3.17 are α=28.22° at the left limit of the profile and α=25.99° at the right limit of

the profile. This procedure was repeated for both the 0.1% and 1.0% surfactant samples. The mean maximum angle allowing detection was 27.27° for 0.1% mixtures and 19.45° for 1.0% surfactant mixtures.

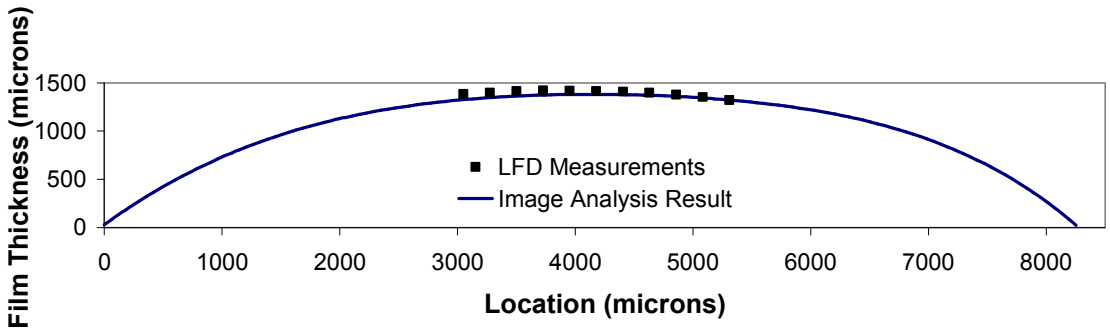

Figure 3.15. Liquid bubble LFD measurements plotted with results from image analysis. (0.1% surfactant mixture)

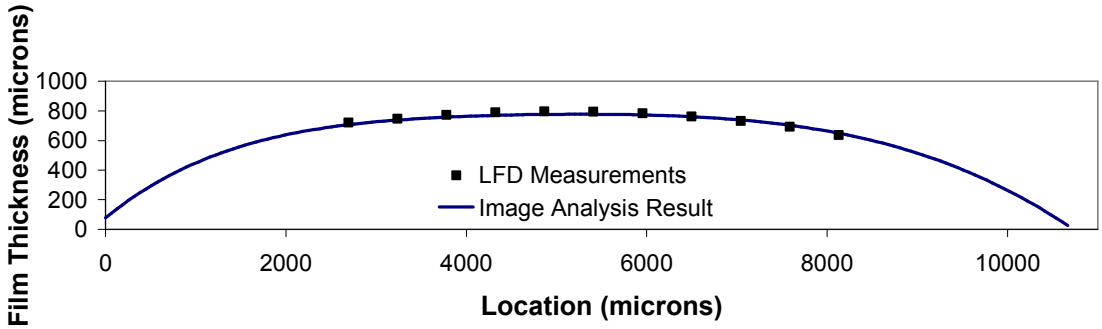

Figure 3.16. Liquid bubble LFD measurements plotted with results from image analysis. (1.0% surfactant mixture)

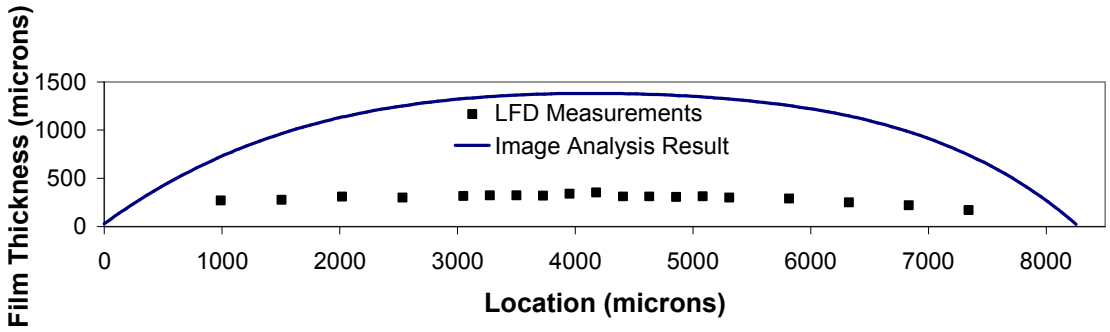

Figure 3.17. LFD measurements of an aluminum-water interface plotted with results from liquid bubble image analysis. (0.1% surfactant mixture)

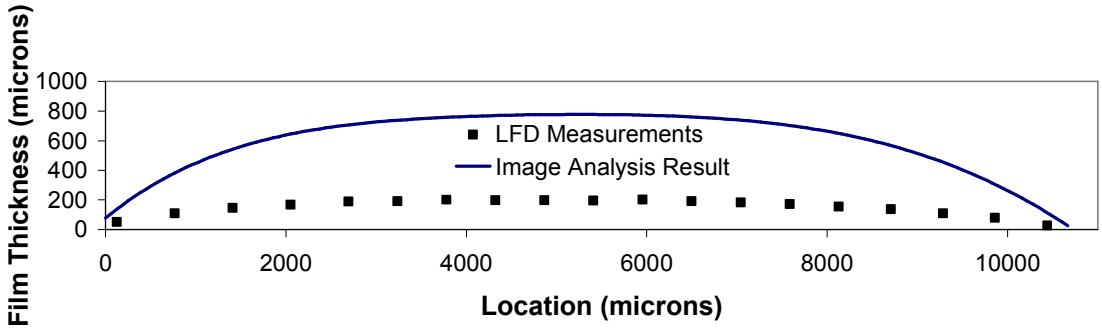

Figure 3.18. LFD measurements of an aluminum-water interface plotted with results from liquid bubble image analysis. (1.0% surfactant mixture)

3.3.6. Minimum Relative Power Prediction. The use of different surfactant mixtures resulted in different surface profiles, and these differences were expected and desired in order to attain a more robust experimental average. When averaging all angle measurements the mean maximum angle allowing detection of the water-air interface was 5.92° with a total uncertainty of ±1.3˚, and the mean maximum angle allowing detection of the aluminum-water interface was 23.36±1.3°. Since the LT-9030 has a cone angle of 23°, these results correspond to α/θ_c=0.257±0.11 and α/θ_c=1.016±0.11 for top and bottom

surface reflection, respectively. The maximum angle results were compared to the relative power calculations, resulting in minimum relative power values of 0.018 and 0.020 for top and bottom surface reflection, respectively. These values are represented by the intersection points shown in Figure 3.19. Thus, the minimum relative power needed for an interface to be detected by the LFD was predicted to be only 1.9% of the incident light's power, P_o. The accuracy of this relative power prediction will greatly depend on the shape of the Gaussian beam intensity profile. If nearly all of the laser's intensity is concentrated in the center of the beam then the maximum angle will be greater than if the laser's intensity is more evenly distributed throughout the radius of the beam. The

Figure 3.19. Relative power plotted versus surface angle divided by laser cone angle. The estimated minimum relative power is shown, including points of intersection.

Gaussian function representing the beam intensity profile will greatly determine the shape of the P/P_o versus α/θ_c curve, and therefore, the validity of the prediction stated above depends on the accuracy of the estimated P/P_o curves when compared to the actual P/P_o values which are determined by the actual beam intensity profile.

3.3.7. Experimental Validation and Results. In order to validate the maximum angle prediction, further experimentation was performed. Optical crown glass with a thickness of 0.2mm along with sapphire disks with thicknesses of 0.508mm, 1.016mm, and 2.032mm were used as the subject pieces in order to isolate the thickness and refractive index effects. Displacement measurements for three different locations on the

Figure 3.20. Thickness measurements for four different subjects when at various angles of orientation.

top surface were made for each subject piece while controlling the angle of orientation, α, on an adjustable stage with an uncertainty of ±0.2°. The LFD mounting apparatus positioned the LFD measuring unit vertically with an uncertainty of ±0.1˚. Thickness is presented in Figure 3.20 in 0.5° increments starting at $\alpha = 0°$ and ending at the maximum measurable angle, where thickness was calculated using Equation (1). The maximum measurable angle was 8° for each of the subject pieces, with the exception of the 1.016mm sapphire disk, which was measurable at 8.5°. In order to investigate how much the measured values are dispersed from the mean thickness, a standard deviation for each set point was calculated as

$$\sigma = \sqrt{\sum \frac{\left(h - \bar{h}\right)^2}{n}} \tag{8}$$

where σ is standard deviation in microns, h is measured thickness in microns, $\bar{h}$ is mean measured thickness in microns, and n is the total number of measured values. Standard deviation results are shown in Figure 3.21 for each subject piece. Figure 3.21 shows that thickness standard deviation increased as α increased, eventually resulting in a large rise in standard deviation before the maximum detection angle was reached. This was expected to result due to the light receiving element detecting less light at higher α which inhibits stable measuring. Although the LFD was not as precise at high α, the mean thickness values remained accurate until the maximum surface angle allowing

Figure 3.21. Measurement standard deviation for four different subjects when at various angles of orientation.

measurement was reached. Thus, the maximum α for sapphire was 8.5±0.55° for both top and bottom surface reflection, which corresponds to α/θ_c=0.370±0.024. The maximum α for optical crown glass was 8.0±0.55° for top and bottom surface reflection, which corresponds to α/θ_c=0.348±0.024. It is important to note that the maximum surface angle allowing measurements was the same for measuring the top and bottom surfaces, and this differs from the liquid bubble measurement results. This discrepancy occurs due to the angle of the bottom surface. In the case of the liquid bubble the aluminum-water interface is at 0° from the horizontal, but for the sapphire and optical crown glass specimens the bottom surface is at the same angle as the top surface, α. In the latter situation, less light is received by the LFD because an angled bottom surface will reflect light away from the

incident beam path as shown in Figure 3.22. This situation involves different geometric calculations than those performed in this study and will not be investigated further because such geometry is uncommon in dynamic film studies. As a result, only the maximum angle allowing measurement of the top surface was used from the sapphire and optical crown glass data.

Figure 3.22. Bottom surface reflection diagram for parallel top and bottom surfaces.

Similar to calculations with water, $\rho(P/P_o)$ versus α/θ_c calculations were performed for sapphire and optical crown glass and the results are shown in Figure 3.23. As stated earlier, α/θ_c=0.370±0.024 at the maximum surface angle for sapphire, which

corresponds to a relative power value of 0.062. α/θ_c=0.348±0.024 at the maximum surface angle for optical crown glass, which corresponds to a relative power value of 0.036. Similar to the prediction of 1.9%, these results show that a very small proportion of the incident light's power must be received by the light receiving element in order to detect an interface. Again, the accuracy of this estimate will greatly depend on the shape of the Gaussian beam profile and the distribution of the laser's intensity throughout the radius of the beam. Imperfections on and in the materials used, or ambient and stray light captured by the light receiving element can also contribute to inaccuracies in this method.

Figure 3.23. Relative power plotted versus surface angle divided by laser cone angle. The estimated minimum relative power is shown, including points representing the maximum measurable angle for each material.

3.4. CONCLUSIONS

Dynamic behavior of the surface angle of a water-air interface will determine how well an LFD can measure film thickness. Any LFD can easily measure the mean thickness of liquid films with steady behavior due to small surface angles. Waves are almost nonexistent in such films. Dynamic films with large waves though, will require an LFD with a large cone angle in order to detect the film surface at locations between the peak and valley of a wave. As noted earlier, a maximum surface angle of 33° was recorded in a study performed by Hazuku et al. [25]. This result is much greater than the maximum angles in this study because Takamasa and Hazuku used an LFD model with a large cone angle (θ_c=43.4°). But, measuring mean film thickness can be adequately performed when only the peaks and valleys of these dynamic films are detected by the LFD. In conclusion, an LFD has the same capabilities of other mean film thickness measuring techniques but its ease of operation gives the technique an advantage. Improvements such as a larger laser cone angle can extend the tool's abilities in situations where the wave profile is desired.

4. EXPERIMENTAL FILM THICKNESS AND SEPARATION MEASUREMENT

Before discussing the experimental procedures and results, this section will proceed by describing the experimental facility. Then, the testing conditions will be discussed, including a description of the three different liquids used to vary surface tension and viscosity, and the rationale for choosing these fluids. The film thickness measurement portion will follow, which includes the experimental procedure and data comparisons with two different computational film propagation models. Finally, the film separation measurement procedure and experimental results will be discussed. The culmination of this study is the film separation results segment, which will include comparisons with two different separation models using various initial conditions.

4.1. EXPERIMENTAL FACILITY

The experimental facility used for this study was designed and built for the investigation of shear-driven thin liquid film propagation and the separation and break-up that occurs at a sharp expanding corner. The facility consists of a four part test section creating a rectangular flow duct, and a schematic of this test section is shown in Figure 4.1.

Gas is pulled from the ambient air through the test section by a liquid ring vacuum pump and gas flow rates through the duct are determined using a laminar flow element (Meriam Model Z50MC2-4). The pressure drop through the laminar flow element is measured by a pressure sensor. Then, an empirical equation supplied with the laminar flow element's calibration details is used to calculate volumetric gas flow rate as a function of the pressure drop. Since the cross sectional area of the duct at the corner is

Figure 4.1. Schematic of experimental test section.

known, the average gas phase velocity at the corner can be calculated using the gas volumetric flow rate. The pump is maintained at a constant speed while an infinitely variable valve is manually controlled downstream from the test section to vary the gas flow rate through the test section. The measured gas flow rate has an uncertainty of less than 3%.

The first of the four test sections, which is not shown in Figure 4.1, is a 1.43 m long entrance region providing for fully developed gas flow at the point of film introduction. The dimensions of the test section in the region from the film inlet to the sharp corner are 2 cm tall by 10 cm wide, giving an aspect ratio of 5. Simulations indicate that, with the 1.43 m entrance region, this aspect ratio should provide two-dimensional flow (i.e. limited wall effects) for the center 7.5 cm of the test section. Consequently, it is over the center 7.62 cm width that the film is introduced. On the bottom wall in the film introduction section a porous medium, which is made of a sintered brass material, allows for liquid introduction without disrupting the flat bottom wall geometry. Liquid flow into the test section is regulated on a volumetric flow basis using a rotometer with an uncertainty of 2.5%. Prior to the rotometer and inlet plumbing, the liquid is contained in a

pressurized tank which is maintained at approximately 620 kPa. Instead of initializing liquid flow by pressurizing the tank or adjusting the rotometer, both of which would result in a gradual increase in volumetric flow rate until the desired rate is reached, the tank pressure is held constant and the rotometer is placed at the desired setting prior to flow. Liquid flow is initialized by the use of an electromagnetic solenoid valve in order to provide for instantaneous flow at the desired flow rate as opposed to a gradual increase in flow that would take place with the use of a manually switched valve.

The sharp corner, which is 23 cm downstream from the film inlet, has an angle of 60° measured from the horizontal. In order to measure film thickness and width proximal to the corner, a glass window is located on the top wall such that optical access is provided 40 mm upstream and 40 mm downstream from the corner. After the corner, the duct has an aspect ratio of 1.429 for the remainder of the test section. The exit section connects to a transitional piece, which connects to 10.2 cm diameter piping. The piping runs to the laminar flow element and then ends at the inlet of the liquid ring vacuum pump, but in between the test section and the laminar flow element a fine wire screen acts as a filter to prevent debris from reaching the laminar flow element.

Preventing biased film flow in the test section is paramount, and the difficulty of achieving symmetric flow across the width of the film has been emphasized in similar experiments [6]. Consequently, proper three-dimensional alignment of the flow duct is given special attention. By building the entire assembly on an optics table, adjustable mounts offer a robust method for supporting and aligning the test section, allowing for small vibrations only. The condition of the porous film introduction material is also

critical for achieving symmetric flow. This inlet piece is replaced when necessary, or the small pores of the material are cleaned in an ultrasonic cleaning bath.

4.2. TESTING CONDITIONS

In order to allow for a variety of flow conditions, the gas phase velocity, film volumetric flow rate, and liquid species were controlled. For this study, gas phase velocities of 20, 30, and 40 m/s and film volumetric flow rates of 6.46, 9.66, 13.01, 16.34, 19.76, and 25.00 cm^3/s were used. These set points resulted in gas phase Reynolds numbers of 24,536, 36,804, and 49,072, and film Reynolds numbers ranging from approximately 100-300. All tests were performed at room temperature which was measured as 19.8 to 21.7˚C for the tests providing this study's results. The ambient pressure was measured as 91.2 to 93.2 kPa. Relative humidity ranged from 37.1% to 52.8%. These changes in ambient conditions were small and were not accounted for in the test results.

Special attention was given to the choice of liquid species in order to control viscosity and surface tension. Also, other fluid characteristics were included in the effort to provide limited problems in the experiment's operation. These included volatility and safety hazards. Each liquid's volatility was important, because film evaporation at the liquid-gas interface reduces the validity of mass conservation laws. The safety information was a significant factor for any fluids considered because it was important to allow the person operating the test to transfer fluids between containers without corrosion or health danger.

Surface tension was critical for obtaining desired flow conditions and also for the ease of experimentation. Water was a simple choice due to its availability, but water has a large surface tension (σ = 0.072 N/m) which caused thicker films and more instability at the edges of shear-driven films. A fluid with a slightly lower surface tension was preferred in order to decrease the amount of film width variation during flow, making film width measurements easier and more reliable. A common mode of decreasing water's surface tension is the addition of surfactants (surface-acting-agents), but surfactants are not always the best solution. In fluid experiments involving separation and/or break-up processes, the surface chemistry of water-surfactant mixtures is not suited for rapid interfacial changes. During these dynamic processes, as the liquid flows and breaks apart, new surfaces are formed. As these new surfaces take shape, the interfacial tension between gas and liquid becomes a dominant force where such an interface did not previously exist and surface chemistry was not important. During separation and/or break-up processes, the surfactant molecules within a water-surfactant mixture must diffuse to new surfaces as new surfaces form. Otherwise, the surfactant is not forming molecular chains at the liquid-air interface, is not fulfilling its role as a surface-acting-agent, and is not affecting the surface tension of water at the new surface. It takes time for surfactant molecules to diffuse to the surface of water as water flows and forms new surfaces, and consequently, the diffusion rate of surfactant in water must be compared with the speed of the separation and/or break processes in this setting. In short, the time scale of surfactant diffusion in water must be compared with the time scale of the separation process. It is uncertain whether surfactant molecules within films can

diffuse to the surface of the film fast enough to maintain a constant surface tension while the separation process occurs.

This time scale problem can only be solved with detailed scrutiny, and was avoided by choosing acetic acid to lower the surface tension of water. Acetic acid molecules (CH_3COOH) are much smaller than surfactant molecules (e.g. Surfynol 400 Series Surfactants: $C_{14}H_{26}O_2(C_2H_4O)_n$) and have much faster diffusion rates in water. Pure acetic acid ($\sigma = 0.027$ N/m) is easily soluble in water, and in fact, vinegar is simply an aqueous solution of acetic acid. Vinegar is approximately 5% acetic acid by volume and was chosen as one of three fluids for this study.

It was desired to vary viscosity while holding surface tension constant. Glycerol has a large viscosity ($\mu = 1500$ cP) and is soluble in water. Also, glycerol has a surface tension quite close to that of vinegar, thus, a glycerol-vinegar mixture was chosen as the second of three fluids. The mixture used was 10% glycerol by mass. Viscosity measurements were made for the glycerol-vinegar mixture by making eight measurements for two trial samples. Also, surface tension measurements were made for the mixture using a tensiometer. Viscosity and surface tension measurement data is presented in Appendix A.

The third fluid was used to vary surface tension while holding viscosity constant. A mineral oil, Conosol C-145, served this purpose well. C-145 is a very lightweight oil with a water-like appearance and has a viscosity of $\mu = 1.421$ cP, which is effectively equal to that of the glycerol-vinegar mixture. Surface tension measurements resulted in $\sigma = 0.027$ N/m. The properties of the C-145 oil, vinegar, and the glycerol-vinegar mixture are presented in Table 4.1.

Table 4.1. Fluid Properties. a – theoretical calculation, b – manufacturer's rating, c – experimental measurement.

Species	Density, ρ (kg/L)	Viscosity, μ (cP)	Surface Tension, σ (mN/m)	Refractive Index, n
Vinegar	1.000[a]	1.010[a]	51.684[c]	1.337[38]
Glycerol-Vinegar Mixture	1.026[a]	1.422[c]	50.135[c]	1.345[39]
C-145 Oil	0.808[b]	1.421[b]	26.524[c]	1.444[b]

4.3. FILM THICKNESS MEASUREMENTS

4.3.1. Measurement Procedure. Shear driven average film thickness measurements were made using a laser focus displacement instrument mounted on the outside of the top wall of the flow duct. Measurements were taken across the width of the film at a location 5 mm upstream from the corner, which prevented film instabilities caused by the corner to influence thickness at the point of measurement. For each flow condition, thickness was measured at evenly spaced locations beginning at one side of the film and extending to the opposite side.

An LFD Model LT-9030 manufactured by Keyence, Co., Japan, was used for this study and specifications for this model are listed in Table 4.2. The LFD system consisted of a measuring unit, which was mounted on a traversing platform above the duct, and a controller, which processed the measuring unit's output signal. The controller was linked with a personal computer and in order to send commands to and receive data from the controller, the computer's Hyperterminal program (Microsoft ® Hyperterminal Version 5.1) allowed for continuous communication. Using certain predetermined command

codes, the operator can record data from the controller in a continuous format. To measure thickness at a film surface location, the focal point of the LFD's beam was placed at the location, and then the operator initiated and ended data recording by Hyperterminal. The result was continuous film thickness data measured at 520.83 Hz for the length of time which Hyperterminal recorded data from the controller. The measuring unit's traversing platform was then translated to a new measurement location and the process was repeated. The traversing platform allowed for 50.8 mm of lateral movement (across the width of the film), and had a resolution of 25.4 μm.

Table 4.2. Laser Focus Displacement Instrument Specifications.

Manufacturer (Model)		Keyence (LT-9030)
Light Source		Visible Red Semiconductor Laser
	Wavelength	670 nm
	Maximum Output	3.0 μm (FDA)
	Classification	Class IIa (FDA)
	Beam Spot Diameter	7 μm
Spatial Resolution		0.1 μm
Measurement Frequency		520.83 Hz
Cycle Time		1.92 ms
Measurement Range		±1.0 mm
Reference Distance		30 mm
Size		94 x 65 x 33 mm
Weight		Approx. 500 g

Measuring thickness at many locations across the width of the film provides valuable cross sectional profile information that is not available in many film studies. As will be shown in this study's film thickness results, a dynamic film's cross sectional

profile is not flat and one must give attention to the variations in film thickness that occur across the width of the film. The utilization of a laser focus displacement instrument provided this study with a simple technique for measuring many locations.

Film thickness measurements required a known bottom wall location relative to the LFD, because thickness was calculated as the difference between the bottom wall location and the film surface location. As a result, film thickness measurement uncertainty is a sum of two measurement uncertainties, the bottom wall and film surface measurement uncertainties. The bottom wall measurement uncertainty includes uncertainty equal to half of the LFD's spatial resolution and an uncertainty caused by the small vibrations inherent in any such facility. Also, the LFD was mounted such that the bottom wall remained a constant distance from the LFD as the unit moved back and forth across the width of the film. Unfortunately though, after great efforts to adjust the LFD traverse such that this distance was constant, an uncertainty of ±5 μm was added to account for cross-directional variations in bottom wall location. Uncertainty from the LFD's spatial resolution was ±0.05 μm and uncertainty from vibrations was ±3 μm, resulting in a bottom wall location uncertainty of ±8.05 μm. Film surface location uncertainty is equal to bottom wall location uncertainty minus the cross-directional variation, which resulted in a total film thickness measurement uncertainty of ±11.1 μm.

A number of data points were removed from the set due to incorrect measurement. If the film surface angle was too large for detection by the LFD, then only the aluminum bottom wall was detected. In order to identify these instances, one of the LFD's extra features was useful. The LFD measures two interfaces simultaneously, and in the case of transparent liquid films, the LFD measures the location of the top and

Figure 4.2. Time resolved film thickness measured using a laser focus displacement instrument.

bottom of the film. Situations where only the bottom surface was detected were easily identified because the top surface location was measured as equal to the bottom surface location. So, any data points showing an equal displacement for the top and bottom surfaces of the film were removed. Thus, dynamic film thickness data presented in this section has been reduced to exclude incorrect measurements resulting from large film surface angles. An example of the measured results after following data reduction procedures is shown in Figure 4.2. In addition, any liquid that splashes onto the optical window refracted the LFD's light, resulting in incorrect measurements. Instead of attempting to identify and exclude these points from the data set, the experiment was temporarily stopped and the glass was cleaned before proceeding. This situation only occurred when high film flow rates were coupled with high gas phase velocities.

Another important note concerns the optical access needed to measure film thickness. The LFD's light beam must travel through flat glass at the top of the flow duct, and this glass does not span the entire width of the test section for structural reasons, limiting optical access for the outer edges of wide films. As a result, the experimental facility did not allow film thickness measurement at the outer edge of the film for any flow conditions which resulted in wide films. The majority of the flow conditions used in this study lie in this category, and film thickness results were presented for any locations where the LFD had optical access to the film.

Film width measurements were also performed for each flow condition. The technique used for measuring width depended on the film width itself. If the width was small enough that the laser's focal point could range from one edge of the film to the other, then the width was measured by placing the focal point on each film edge and recording the position of the LFD. This technique resulted in a film width uncertainty of ±0.762 mm. In cases of large film width, which included most flow conditions, the width was measured using calipers with a resolution of 0.25 mm. This method included notable uncertainty caused by parallax, resulting in a total film width uncertainty of ±3.25 mm.

4.3.2. Results. A short discussion of film width results will be presented first in order to establish a few general relations prior to discussing film thickness details.

4.3.2.1. Film width. The film width measurements provided simple indications of the ways different flow conditions influenced film flow. The most dominant correlations were that of gas phase velocity and film flow rate with film width. Figure 4.3 shows film width plotted versus film flow rate for gas phase velocities of 20, 30, and 40 m/s for vinegar. As gas phase velocity increases, film width increases. For example,

Figure 4.3 shows a film flow rate of 6.46 cm^3/s resulted in film widths of 39.37 mm, 52.07 mm, and 59.69 mm for gas phase velocities of 20, 30, and 40 m/s, respectively. From Figure 4.3, one can also observe that a trend of increasing width also appears for an increasing film flow rate. Figure 4.4 shows a similar plot for the glycerol-vinegar mixture, and the same relationships appear. Viscous effects on film width can be determined by comparing Figures 4.5, 4.6, and 4.7, which compare vinegar and glycerol-vinegar film widths for each gas phase velocity. It is shown that at particularly low film flow rates the higher viscosity of the glycerol-vinegar mixture results in wider films.

Film width effects due to surface tension could not be quantified with the fluids used in this study. Oil films made contact with the side walls of the flow duct even at the lowest film flow rates and gas phase velocities. These dramatically wider oil films resulted due to a large decrease in surface tension characterized by the oil. The oil film was not expected to contact the side walls for low film flow rates, but it was concluded that this occurred due to the effects of higher viscosity on width at low film flow rates, as was discussed above for the glycerol-vinegar mixture.

4.3.2.2. Film thickness. Film thickness measurements were made across the width of the film at 21 points located 5 mm upstream from the corner. For a few particular flow conditions, more than 21 locations were measured in order to provide a more detailed view of the cross sectional profile of the film. Two of these flow conditions are presented in Figure 4.8 in order to introduce the general shape of a shear-driven liquid film. All film thickness results are presented such that the *x*-axis ranges from zero at the left side wall of the flow duct to 100 mm at the right side wall. Figure 4.8 shows two very different flow conditions, but both result in a similar film surface shape. For any

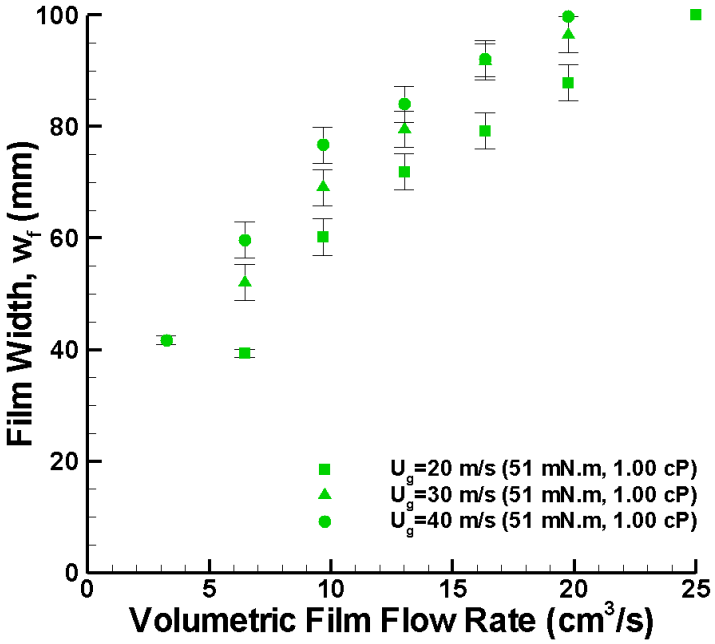

Figure 4.3. Film width plotted versus volumetric film flow rate for vinegar at various gas phase velocities.

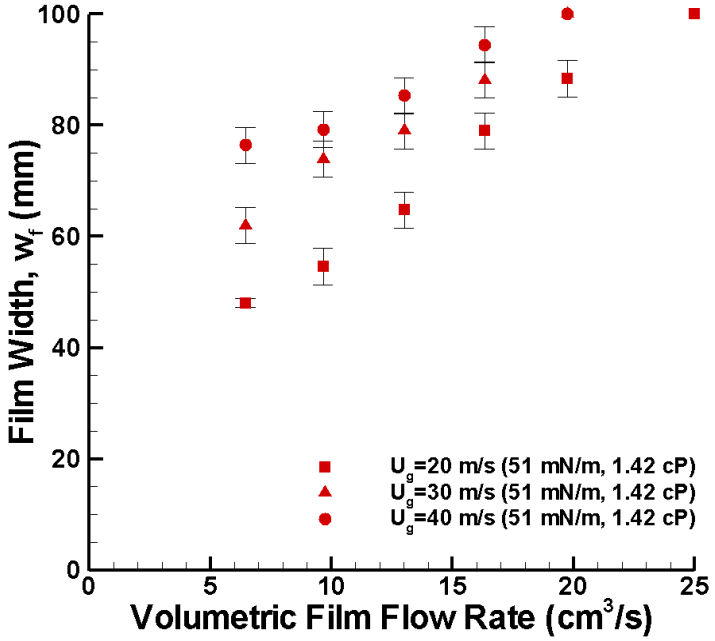

Figure 4.4. Film width plotted versus volumetric film flow rate for the glycerol-vinegar mixture at various gas phase velocities.

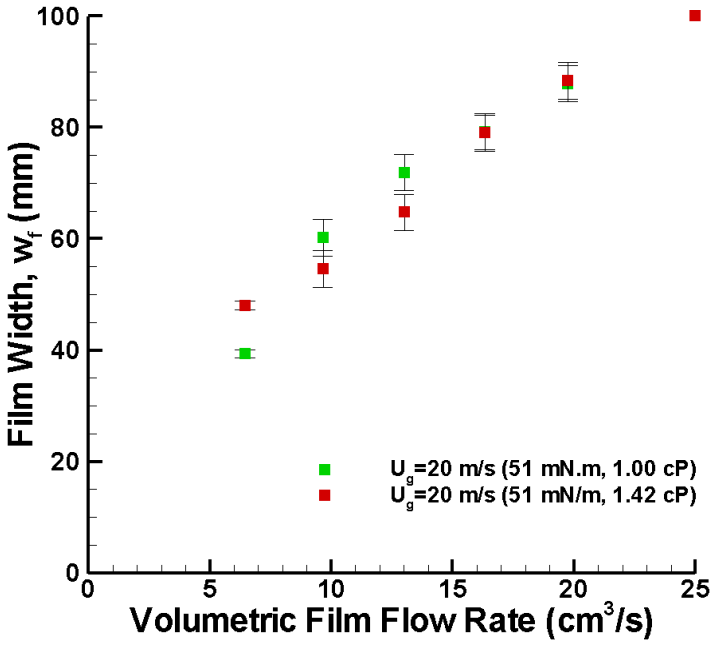

Figure 4.5. Film width plotted versus volumetric film flow rate at a gas phase velocity of 20 m/s, showing fluids with different viscosity values.

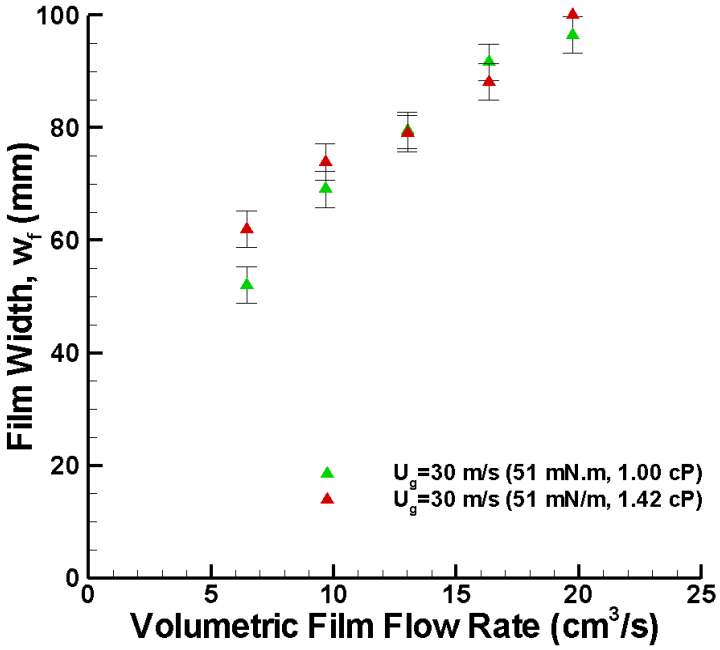

Figure 4.6. Film width plotted versus volumetric film flow rate at a gas phase velocity of 30 m/s, showing fluids with different viscosity values.

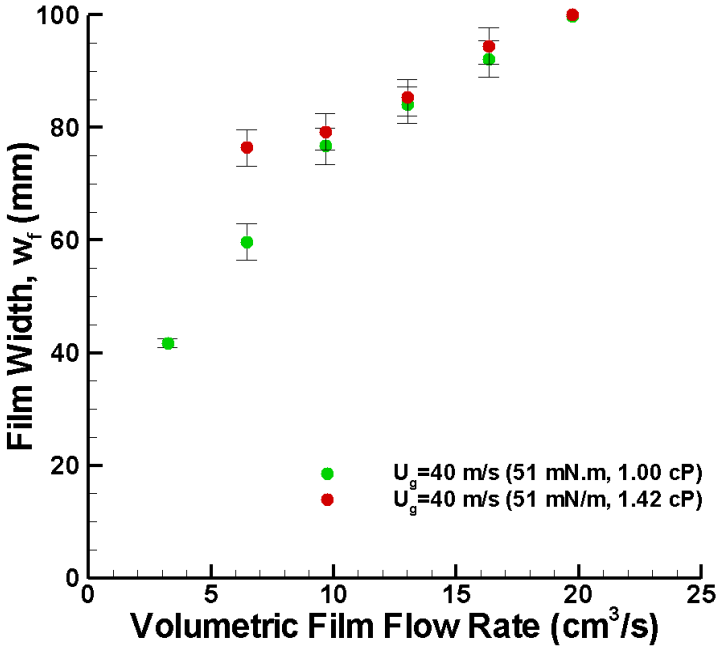

Figure 4.7. Film width plotted versus volumetric film flow rate at a gas phase velocity of 40 m/s, showing fluids with different viscosity values.

combination of the different fluids, gas phase velocities, and volumetric flow rates used in this study, the same general film shape formed. In many of the film thickness plots presented in this study, the thickest portions of the film are not shown due to a lack of optical access, which was discussed in *4.3.1. Measurement Procedure.* Though, the film edge is included in all film thickness plots. With the exception of the outer edges of the film, the thinnest part of the film occurs in the center and the thickest part occurs near the edges. This happens due to surface tension. The surface tension of the film resists cross directional expansion of the film width, while surface shear stress and gravity push the film outward and downward. The result is a conglomeration of coherent liquid near the film edge. Concerning the *leading* edge of the film, this study focuses on the behavior of

fully developed flows, so the behavior of the leading edge of the film in the stage of initial propagation was not investigated.

Figure 4.8. An example of film thickness measured across the width of the film.

In the environment of liquid films, adding an adjacent gas phase flow results in a film with characteristics greatly dependent on gas phase velocity. In particular, gas phase velocity has a significant effect on film thickness, and these effects are presented in Figures 4.9-4.14. Figures 4.9-4.14 show film thickness for all three gas phase velocities used in this study: 20, 30, and 40 m/s. Film thickness of vinegar is shown in Figures 4.9 and 4.10 for a volumetric film flow rate of 6.46 and 19.76 cm^3/s, respectively. Results are shown in the same format for the glycerol-vinegar mixture and oil in Figures 4.11-4.14.

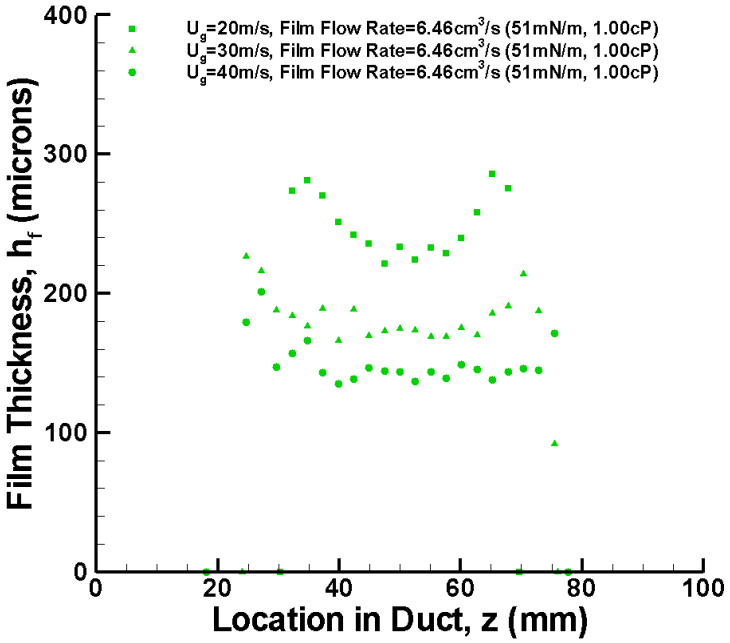

Figure 4.9. Measured film thickness of vinegar for various gas phase velocities at $\dot{\forall}_f = 6.46$ cm^3/s.

Figure 4.10. Measured film thickness of vinegar for various gas phase velocities at $\dot{\forall}_f = 19.76$ cm^3/s.

Figure 4.11. Measured film thickness of the glycerol-vinegar mixture for various gas phase velocities at $\dot{\forall}_f = 6.46$ cm^3/s.

Figure 4.12. Measured film thickness of the glycerol-vinegar mixture for various gas phase velocities at $\dot{\forall}_f = 19.76$ cm^3/s.

Figure 4.13. Measured film thickness of oil for various gas phase velocities at $\dot{\forall}_f$ = 6.46 cm^3/s.

Figure 4.14. Measured film thickness of oil for various gas phase velocities at $\dot{\forall}_f$ = 19.76 cm^3/s.

The results show that as gas phase velocity increases, film thickness decreases. This phenomenon was observed for all three fluids and all volumetric flow rates used in this study, and occurred due to the increase in shear stress at the film surface, resulting in an increase in film velocity. For a particular volumetric film flow rate, if the film velocity increases then the cross sectional area of the film must decrease to conserve mass. Thus, film thickness decreases for an increase in gas velocity.

An increase in the overall quantity of liquid that flows through the system will logically affect the film thickness. Thus, volumetric film flow rate also influenced film thickness. The effects of volumetric film flow rate on film thickness are presented in Figures 4.15-4.20, where each figure shows film thickness results for volumetric film flow rates of 6.46, 13.01, and 19.76 cm^3/s for one fluid at one gas phase velocity. As film flow rate increases then film thickness increases, and this trend occurs for all gas phase velocities and fluids used in this study.

Surface tension influences film thickness indirectly. Surface tension influences the width of a film because the location of the edge of the film greatly depends on the interfacial forces acting at the edge. As film width changes, film thickness changes due to the expansion or retraction of the outer edge of the film, resulting in mass transfer from the center of the film to the outer edge or vise versa. For example, large surface tension will result in narrow films where liquid forms a more coherent mass near the center of the flow duct, but small surface tension allows the liquid to spread across the bottom wall of the duct forming wide films. Consequently, smaller surface tension causes thinner films, which is reflected by Figure 4.21. Figure 4.21 shows film thickness for different fluids at identical flow conditions in order to isolate surface tension effects.

Figure 4.15. Measured film thickness of vinegar for various film flow rates at U_g = 20 m/s.

Figure 4.16. Measured film thickness of vinegar for various film flow rates at U_g = 40 m/s.

Figure 4.17. Measured film thickness of the glycerol-vinegar mixture for various film flow rates at U_g = 20 m/s.

Figure 4.18. Measured film thickness of the glycerol-vinegar mixture for various film flow rates at U_g = 40 m/s.

Figure 4.19. Measured film thickness of oil for various film flow rates at U_g = 20 m/s.

Figure 4.20. Measured film thickness of oil for various film flow rates at U_g = 40 m/s.

Figure 4.21. Measured film thickness of fluids with different surface tension.

Figure 4.22. Measured film thickness of fluids with different viscosities.

Another dominant flow parameter influencing film behavior is film viscosity. White [40] explains that viscosity associates "with the ability of a fluid to flow freely." Thus, we should expect variations in film viscosity to directly affect film velocity. Much of the viscosity effects will be discussed after presenting average film velocity data in *4.3.2.3. Film Velocity*, but brief conclusions can be made regarding viscosity effects on film thickness. Viscosity is isolated in Figure 4.22 by holding gas phase velocity and film flow rate constant for fluids with different viscosities: vinegar and the glycerol-vinegar mixture. Also, both of the flow conditions presented in Figure 4.22 resulted in the same film width, which makes this particular flow condition ideal for isolating the affect viscosity has on film thickness. In this illustration, film thickness is greater for the glycerol-vinegar mixture because of its higher viscosity. It is expected that the glycerol-vinegar mixture will move slower than vinegar at a given volumetric flow rate and gas phase velocity, so the outcome is a greater cross sectional area for the glycerol-vinegar mixture than vinegar in order for both to support the same volumetric film flow rate. These viscosity conclusions will be ameliorated by the average film velocity results presented next.

4.3.2.3. Film velocity. As mentioned above, the volumetric film flow rate and the cross sectional area of the film can be related to estimate the average film velocity. More specifically,

$$\bar{u}_f = \frac{\dot{\forall}_f}{A_f} \tag{9}$$

where $\bar{u}_f$ is the average film velocity, $\dot{\forall}_f$ is the volumetric film flow rate, and A_f is the cross sectional area of the film. This relation was used with the experimental film thickness results to estimate the average film velocity, $\bar{u}_f$.

The volumetric film flow rate was a controlled parameter in this experiment, and thus was known for all flow conditions. But, values used for film area, A_f, must be estimated using the film thickness data available for each flow condition. In cases where film thickness was measured across the entire width of the film, including both edges, the film area can be accurately calculated using the trapezoidal rule. The trapezoidal rule uses a closed integration formula to find the area under a curve depicted by finite data points, such as the measured film thickness data points which embody the film surface. For this application, the trapezoidal rule takes the form

$$A_f = \sum_{i=1}^{i_{\max}-1} (z_{i+1} - z_i) \frac{h_f(z_i) + h_f(z_{i+1})}{2} \tag{10}$$

where the film area is calculated as the sum of the areas in between each adjacent pair of film thickness data points. The sum begins at a data point representing the left edge of the film where $i=1$, and proceeds to a data point representing the right edge of the film where $i=i_{max}$. The spanwise location within the flow duct is denoted as z_i. For example, $h_f(z_1) = 0$ and $h_f(z_{i_{\max}}) = 0$, because the film thickness at the edge is zero. The trapezoidal rule was employed for low flow conditions, where the film width was small enough to allow complete optical access to the film.

A second, more crude method was used to calculate film area for flow conditions where the outer edges of the film could not be measured, which included most flow conditions. This method defined area as the product of film width, w_f, and average film thickness, $\bar{h}_f$:

$$A_f = w_f \bar{h}_f \ . \tag{11}$$

Film width was measured directly as discussed earlier, while average film thickness was calculated as a mean of all thickness data points across the width of the film. Since the average film thickness method only applied to cases where the outer edges of the film were not measured, then by default, $\bar{h}_f$ was a mean thickness for the relatively flat center of the film.

When closely examining the cross sectional profile of the film surface, it is clear that there are significant variations in film thickness across the width of the film. Thus, calculating the cross sectional area of the film using (11) may not be viable. Consequently, a question arises: How much accuracy is lost when the more definitive trapezoidal rule must be replaced by the average thickness method? To address this issue, calculations executed with the average film thickness method, (11), were compared to calculations carried out with the trapezoidal rule, (10). For 9 of the 48 total flow conditions, the trapezoidal rule was applied because film thickness measurements were available for the complete width of the film. For these 9 conditions, film area was found using (10), and also (11) where $\bar{h}_f$ was a mean thickness for the flat center of the film.

Thus, although outer edge thickness data was available, the outer edges of the film were not used when calculating mean thickness. With this procedure, the film area resulting from each technique was compared to check the validity of the average film thickness method. The percent difference between the areas calculated using each technique was relatively small. The mean percent difference for these 9 flow conditions was 4.58%, and it was concluded that although the trapezoidal rule offers a more detailed analysis, little accuracy is lost by using the middle portion of the film to approximate the entire cross sectional film area. After establishing the area calculation regiment, the average film velocity, $\bar{u}_f$, was calculated for each flow condition. Similar to the manner which film thickness data was presented, velocity discussions will proceed by discussing gas phase velocity effects, volumetric film flow rate effects, surface tension effects, and then viscosity effects.

As expected, gas phase velocity directly affected average film velocity. Figures 4.23, 4.24, and 4.25 show film velocity for vinegar, the glycerol-vinegar mixture, and oil, respectively. First, it is evident that film velocity increases as gas phase velocity increases due to an increase in the shear stress at the surface of the film. Second, a direct relationship between film velocity and film flow rate also appears. The average film velocity increases with an increase in film flow rate, which is an elementary concept, but a closer look at the results reveals that the slope of this trend is influenced by gas phase velocity, film viscosity, and surface tension.

As shown by Figures 4.23, 4.24, and 4.25, an increase in gas phase velocity results in a change in the slope of the $\bar{u}_f$ versus $\dot{\forall}_f$ trends. This slope can be referred to

as $\frac{\partial \overline{u}_f}{\partial \dot{\forall}_f}$. All three of the fluids used in this study reveal that increasing the gas phase velocity causes an increase in $\frac{\partial \overline{u}_f}{\partial \dot{\forall}_f}$. Changing viscosity or surface tension has a similar effect. Figures 4.26, 4.27, and 4.28 show that when the film viscosity was increased from 1.00 to 1.42 cP $\frac{\partial \overline{u}_f}{\partial \dot{\forall}_f}$ increased, and the same result occurred when surface tension was decreased from 51 to 27 mN/m. These trends, caused by fluid properties, are consistent for all gas phase velocities used in this study.

Disregarding the slopes discussed above, one should be able to make more simple conclusions regarding the effects of fluid properties on the absolute values of average film velocity. First, surface tension effects were evident in the oil, in which σ = 27 mN/m. The low surface tension caused the oil to have a smaller velocity than that of vinegar or the glycerol-vinegar mixture, where σ = 51 mN/m. This phenomenon occurred due to the large film width achieved by the oil due to a low surface tension, increasing the overall cross sectional area, A_f, of the film. Since increasing A_f while holding $\dot{\forall}_f$ constant causes a decrease in average film velocity per (9), the oil maintained a lower velocity for nearly all flow conditions. Concerning the effects of viscosity, it was expected that increasing film viscosity would result in an overall decrease in film velocity due to an increase in shear stress, τ, within the film:

$$\tau_{xy} = \mu_f \frac{\partial u_f}{\partial y}. \tag{12}$$

Figure 4.23. Average film velocity of vinegar for various gas phase velocities.

Figure 4.24. Average film velocity of the glycerol-vinegar mixture for various gas phase velocities.

Figure 4.25. Average film velocity of oil for various gas phase velocities.

Figure 4.26. Average film velocity of all three fluids for U_g = 20 m/s.

Figure 4.27. Average film velocity of all three fluids for U_g = 30 m/s.

Figure 4.28. Average film velocity of all three fluids for U_g = 40 m/s.

This expectation was not consistently shown in the results, though. One can point to two elements as the source of this inconsistency. First, the change in viscosity is relatively small, $\Delta\mu_f = 0.42$ cP. Second, changes in film width and/or thickness will indirectly affect the average film velocity by changing the film's cross sectional area, and since film width and thickness cannot be held constant between different fluids, these changes inhibit the isolation of viscosity effects. It is believed that the combination of these two factors prevented a repeatable difference in $\overline{u}_f$ for vinegar and the glycerol-vinegar mixture.

To conclude, one will best understand the validity of the average film velocity data by understanding the uncertainties involved. The average velocity results presented above greatly rely on conservation of mass for the liquid film. The volumetric film flow rate, $\dot{\forall}_f$, is controlled by a rotometer located before the film introduction point, and the same volumetric film flow rate value is assumed viable for film flow at the corner. As mentioned in *4.2. TESTING CONDITIONS*, the film's volatility was an important factor in choosing the fluids for this experiment. If a fluid such as gasoline or ethanol was chosen, then film evaporation within the test section would encumber conservation of mass, increasing uncertainty for average film velocity calculations. Thus, although these fuels are present in important shear-driven applications they could not be utilized here due to high volatility. As shown by the error bars in Figures 4.23-28, the uncertainty accompanying the average film velocity calculations are especially large for high flow rates, so choosing a fluid with low volatility was a must. Otherwise, uncertainties within the average velocity calculation, which is a critical part of any film separation criterion, would be too large. The uncertainty of this calculation increased with an increase in

volumetric film flow rate due because the rotometer uncertainty was a percentage of the flow rate, thus increasing as flow rate increased. In addition, the uncertainty of the velocity calculation increased with an increase in gas phase velocity. This occurred because average film velocity is highly dependant on film thickness, and as gas velocity increased then the film thickness decreased, thus making the thickness measurement uncertainty (±11.1 μm) larger in relation to the film thickness. It also must be noted that the velocity throughout the thickness of the film is not constant. The velocity is expected to be greatest at the film surface, where the adjacent gas phase flow is acting on the film, and the velocity will be smallest at the bottom wall. Thus, the average film velocity calculation cannot describe this velocity gradient, but appropriately fulfills the intended purpose of estimating the average flow conditions at the corner as initial conditions for a film separation model.

4.3.3. Comparisons with Computational Models. The experimental results offer a valuable baseline for validating computational tools. Two computational fluid models will be compared with the experimental results discussed above. Since both of the modeling regimes investigated here are not three-dimensional, but instead two-dimensional simulations, then variations in film width and cross sectional film area will not be investigated by the simulations. The main purpose of these validations is to find a computational methodology that can accurately predict the time-averaged thickness and velocity of a shear-driven film. If confirmed as sufficiently accurate, then the computed mean values can be used as initial conditions for a model predicting film separation. Given that film separation models such as the Force Ratio of Friedrich et al. [35] and the radial stress model of Owen and Ryley [27] analyze the flow in a time-averaged two-

dimensional sense, then three-dimensional film computations, which add film width and cross sectional profile information, may or may not be necessary for producing accurate film thickness and velocity values. Of the simulations investigated here, one model is a shear-driven film propagation model proposed by Sattelmayer and Wittig [41], which treats the liquid film as a rough wall interacting with the gas flow at the interface. This model will be referred to here as the Rough Wall Model. First though, results and comparisons for the Volume of Fluid model will be discussed.

4.3.3.1. Volume of Fluid model. FLUENT is a computational fluid dynamics software package which offers a variety of physical models that apply to an array of industries. Within the FLUENT platform, the existing Volume of Fluid model (VOF) component combined with a selected turbulence model was used to simulate the experimental apparatus exactly as described in *4.1. EXPERIMENTAL FACILITY*.

The VOF computational technique has been utilized for two phase flow by Thiruvengadam et al. [42] for two-dimensional simulation and by Buelow et al. [43] and most recently Lan et al. [44] for three-dimensional simulation. The VOF model is built such that the interface between different phases can be located by determining the volume fraction of fluid species in each computational cell of a fixed Eulerian mesh. The volume fraction of the liquid phase (film) is denoted as α_f and varies between zero and one. Thus, the two phase flow is simulated as pseudo-single phase flow with variable properties, such as density and viscosity. In this format, the liquid volume fraction in each computational cell determines the properties of the mixed fluid by using the properties of each individual phase. As a result, the density and viscosity of the mixed fluid vary with position because volume fraction varies with position. The liquid volume

fraction for each grid cell is used to determine the location of the interface between phases, which is needed to determine film thickness.

The surface tension coefficient of the film-air interface is used within the VOF model. It was shown in the experimental results that surface tension influenced the film width, but if this computational scheme is two-dimensional (i.e. ignoring film width variations) then how does surface tension influence film thickness and velocity? In the VOF model, the surface tension force is dependent on the surface tension of the interface and the gradient of the liquid volume fraction. Since surface tension forces are not acting at a film edge as in a three-dimensional scheme, then surface tension forces will only have influence on interface curvature, which occurs at a change in film thickness. The VOF model results yield a relatively flat film surface, with the exception of the film inlet region and the corner region, where the *y* component of the film velocity is changing. Figures 4.29 and 4.30 show the VOF model's results for a low flow condition (U_g = 20 m/s, $\frac{\dot{\forall}_f}{w_f}$ =1.71 cm^2/s, μ_f = 1.00 cP, σ = 51 mN/m) and a higher flow condition (U_g = 30 m/s, $\frac{\dot{\forall}_f}{w_f}$ =2.59 cm^2/s, μ_f = 1.00 cP, σ = 51 mN/m), respectively. As the film flows over the corner, the film surface, which is flat before the corner, changes location due to effects at the corner. Consequently, the film surface curvature increases at the corner, and a high surface tension will amplify this effect more than a low surface tension. The VOF model's film thickness results were determined 5 mm before the corner, corresponding to the experimental measuring location. If the fluid's surface tension is high, then corner effects may slightly influence the film thickness 5 mm before the corner to facilitate surface continuity. Considering the surface tension values used in this study, surface

Figure 4.29. The computational results of the Volume of Fluids model for U_g = 20 m/s and $\frac{\dot{\forall}_f}{w_f}$ = 1.71 cm^2/s, with surface curvature upstream from the corner.

Figure 4.30. The computational results of the Volume of Fluids model for U_g = 30 m/s and $\frac{\dot{\forall}_f}{w_f}$ = 2.59 cm^2/s, with surface curvature upstream from the corner.

tension should have a small, almost negligible effect on thickness variation between fluids in the two-dimensional VOF scheme.

A low-Reynolds k-ε turbulence model was used to simulate the turbulence in the flow. The SIMPLE algorithm was used to deal with the coupling computations between the flow field and the pressure field. Both of these configurations are options within the FLUENT software package.

The geometry was identical to the experimental test section beginning at a location 0.0127 m upstream from the liquid inlet and ending at the downstream end of the exit section shown in Figure 4.1. At the gas flow inlet (x = 0 m), the results of the independent two-dimensional air turbulence simulation mentioned above provided a fully developed air flow for the inlet boundary conditions. The result was inlet mean gas phase velocities of 20, 30, or 40 m/s to match the flow conditions used in the experimental work. At the film inlet located on the bottom wall (0.0127 m < x < 0.0254 m), a uniform film velocity normal to the air flow was used as the boundary condition. The initial film velocity in the x direction was zero (u_f = 0). The width and length of the experimental test section's film inlet region (0.0127 m x 0.0762 m) were used with the experimental volumetric film flow rates in order to calculate the corresponding film inlet velocities for the computational regime. More specifically,

$$v_f = \frac{\dot{\forall}_f}{(0.0127m)(0.0762m)} \tag{13}$$

where v_f is the uniform film velocity (m/s) in the y direction at the film inlet, and $\dot{\forall}_f$ corresponds to the volumetric film flow rate (m^3/s) used in the experimental work.

The film thickness solution was the parameter of interest, so a small cell size was used in the region occupied by the film in order to offer more accuracy in determining the film-air interface. The smallest mesh size was located at $y < 500$ μm, where $y = 0$ at the bottom wall. The mesh then gradually transitioned to a coarser mesh as y increased to the areas occupied by gas flow.

Computationally, it was necessary to limit the change in each variable between iterations, which is under-relaxation. Under-relaxation factors were used with all the variables for better numerical stability. There was a large difference in the properties of the two fluids, and as a result, the relaxation factors for density and body force are chosen to be 0.5, and the relaxation factors for momentum and volume fraction are chosen as 0.4. In computational methods which involve multiple iterations, each iteration will not provide an exact solution for all governing equations. For this reason, residual quantities are tracked for each iteration, providing a gauge of accuracy for the variable values at that iteration. For this study, a converged solution was achieved when the volume fraction residual was between 1×10^{-5} and 3×10^{-5}. To ensure that these residual values were small enough to guarantee a converged solution, a residual study was performed to confirm that residuals of less than 1×10^{-5} were not necessary to reach a stable solution. The residual study results shown in Table 4.3 indicate that when the volume fraction residual was on the order of 10^{-5}, further change in the residual value caused a small change in film thickness.

Table 4.3. Volume fraction residual study.

Iterations	Volume Fraction Residual Value	Film Thickness, h_f (μm)
40,000	8.0×10^{-5}	266.60
50,000	4.1×10^{-5}	269.07 (+0.93%)
70,000	8.4×10^{-6}	283.44 (+5.34%)

In order to extract film thickness values from the VOF model's computational results, the film-air interface was located. The location of this interface depended on the liquid volume fraction, α_f. Different choices of α_f ranging from zero to unity will result in variation in the amount of the total injected liquid mass flow rate that is included under the interface. In a similar shear-driven film study made by Lan et al. [44], it was shown that 88% of the injected liquid film mass flow rate was captured if the interface was placed at a liquid volume fraction line of $\alpha_f = 0.5$. Similarly, 90% of the injected liquid film mass flow rate was captured when $\alpha_f = 0.4$. Consequently, since decreasing the liquid volume fraction from 0.5 results in very small changes in the captured mass flow rate, then for this study $\alpha_f = 0.5$ was used to locate the film-air interface, and thus, the film thickness.

In order to validate the VOF model as a shear-driven film simulator for the test section used in this study, the computed film thickness results are compared with the experimentally determined film thickness values. This comparison is presented in Figures 4.31, 4.32, and 4.33 for gas phase velocities of 20, 30, and 40 m/s, respectively. First and foremost, it should be reiterated that the VOF model is a two-dimensional model, not

accounting for any changes in film width or any thickness variations across the width of the film. The experimental facility though, allowed for three-dimensional effects to greatly affect film flow. After liquid was injected through the film inlet region of the test section, the liquid film was permitted to increase in width, spreading across the bottom wall of the test section. Consider, for a moment, an experimental facility constructed such that the film injection region had the same width as the entire bottom wall, stretching from one side wall to the other side wall. A two-dimensional computational model may be more suited to predict film flow parameters for such an apparatus, because the side walls will not allow the film to increase in width as it propagates across the bottom wall.

Figure 4.31. Average film thickness as simulated by the Volume of Fluids model plotted with the experimentally measured values of all three fluids for U_g = 20 m/s.

Figure 4.32. Average film thickness as simulated by the Volume of Fluids model plotted with the experimentally measured values of all three fluids for U_g = 30 m/s.

Figure 4.33. Average film thickness as simulated by the Volume of Fluids model plotted with the experimentally measured values of all three fluids for U_g = 40 m/s.

Thus, much of the three-dimensional effects would be eliminated, favoring the use of a two-dimensional model. So, after considering the dimensional difference, the comparisons were plotted using a two-dimensional flow rate on the *x*-axis. The volumetric flow rate of the film, $\dot{\forall}_f$, was normalized using the film width, $\frac{\dot{\forall}_f}{w_f}$. But, in this case, when the experimental film thickness results are compared to the VOF model, Figures 4.31, 4.32, and 4.33 show that the model over estimated film thickness, generally. For a given flow condition, if the film width was measured to be approximately equal to the width of the film injection region (w_{fo} = 76.2 mm), then film thickness predicted by the VOF model was closer to the measured value. This occurs at low film flow rates (e.g. $\dot{\forall}_f$ = 6.46 cm^3/s). This dimensional effect was assumed to be avoided by using a two-dimensional flow rate, $\frac{\dot{\forall}_f}{w_f}$, so there may be other theoretical problems with the VOF model.

Concerning the influence of fluid properties (σ and μ_f) on the VOF model's results, it was stated that surface tension should have a negligible affect on the film thickness due to the two-dimensional format. This conjecture was held true by the small difference in values for the glycerol-vinegar mixture (σ = 51 mN/m) and the oil (σ = 27 mN/m). The film thickness results showed that a lower surface tension tends to cause slightly thicker films, and this trend was very consistent for gas phase velocities of 30 and 40 m/s. This tendency can be explained by the curvature of the film at the corner in the VOF simulation. As liquid flows passed the corner, the downward change in flow direction causes the film to form a rounded surface, which decreases the thickness of the

film immediately before the corner. This phenomenon is shown in Figure 4.29, and again in Figure 4.30 for the case of separation. Since the film thickness values drawn from the VOF model were taken at a location 5 mm before the corner, then the decrease in thickness due to corner effects should be negligibly small. Surface tension though, can influence how large or small this effect truly is. When comparing surface tensions of 27 and 51 mN/m, the higher surface tension force should cause the surface curvature at the corner to have a slightly larger affect on the thickness 5 mm before the corner. Thus, the film thickness of the glycerol-vinegar mixture was slightly smaller than that of the oil when simulated by the VOF model.

The effects of film viscosity can be made clear by investigating the model's velocity results rather than the thickness results. A simple method was used to determine the average film velocity of the VOF model results. To allow for a comparison with the experimentally inferred average film velocity data exhibited in *4.3.2.3. Film velocity*, the average film velocity results of the VOF model were calculated by dividing the two-dimensional film flow rate, $\dot{Q}_f$, by the film thickness:

$$\overline{u}_f = \frac{\dot{Q}_f}{h_f}. \tag{14}$$

This calculation was executed for each flow condition, resulting in the average film velocity results presented in Figures 4.34, 4.35, and 4.36, where VOF computations are compared with experiments. When comparing the VOF computations with experimental results, the VOF model tends to under estimate the film velocity, which correlates with

the over estimation of film thickness discussed earlier. Viewing the VOF model's velocity computations alone, it is apparent that the film velocity is highest for vinegar, which is expected due to its low viscosity (μ_f = 1.00 cP). This difference is relatively small, but only a small difference should exist because the viscosity of the remaining two fluids is only 0.42 cP higher.

As mentioned earlier, other investigators have used the VOF model for shear-driven films. Thiruvengadam et al. [42] computed two-dimensional simulations and compared the film thickness and velocity results with the experimental data of Wittig et al. [8]. For all three gas phase velocities used in their study (U_g = 30, 60, and 90 m/s), the

Figure 4.34. Average film velocity as simulated by the Volume of Fluids model plotted with the experimentally determined values of all three fluids for U_g = 20 m/s.

Figure 4.35. Average film velocity as simulated by the Volume of Fluids model plotted with the experimentally determined values of all three fluids for U_g = 30 m/s.

Figure 4.36. Average film velocity as simulated by the Volume of Fluids model plotted with the experimentally determined values of all three fluids for U_g = 40 m/s.

experimental film thickness measurements of [8] were 25-50% thicker than the VOF model predictions of [42]. The under estimation of film thickness in [42] is inconsistent with the over estimation that was presented for the current study. Assessing this difference, it is believed that the difference in experimental technique between the current study and that of Wittig et al. [8] is the source of the discrepancy. Wittig et al. [8] did not investigate the cross sectional profile of the film as in this study. Instead, one thickness measurement was made at the center of the film and this value was used as a good approximation of the entire film width. Also, film was permitted to contact the side walls of the flow duct, constraining liquid to fill up the bottom of the test section instead of allowing the film to spread across a wider flow duct as in the current study.

The work of Lan et al. [44] involved three-dimensional VOF model computations, and the results were compared to experimental film width and thickness measurements made using a laser interferometry technique. The results of both the thickness and width comparisons were agreeable. The accuracy of these computations can be explained by the three-dimensional nature of the simulations. Using a laser interferometry method, film thickness was measured only in the spanwise center location of the duct, but Lan et al. [44] compared this measurement with the film thickness corresponding to the same location within the three-dimensional simulation. Cross sectional variations in film thickness were accounted for, because a specific spanwise location was used for the comparison.

In conclusion, the inaccuracy of the current study's computations may lie in the two-dimensional approach. Past validations of the VOF model's accuracy in simulating shear-driven films resulted in better agreement, but this occurred due to either a

dimensional constraint within the experimental technique [42] or the appropriate three-dimensional correspondence between experiments and computational simulation. If the VOF model is to be used for predicting time-averaged film thickness and velocity, then it is recommended that a three-dimensional domain be used in order to accurately mimic the three-dimensional nature of the experiment.

4.3.3.2. Rough Wall Model. The Rough Wall Model is a computational fluid dynamics (CFD) model developed to simulate the flow of shear-driven films. The "rough wall" terminology is rooted in the way the model treats the film as a rough wall which interacts with the gas phase flow. The wall roughness is computed as a function of the interfacial shear stress and the average film thickness, and thus, the wall roughness offers a mode of interaction between the gas flow and the liquid film flow. The calculation of the gas flow is based on the Reynolds-averaged Navier-Stokes (RANS) equations and a standard k-ε turbulence model is used. The liquid film flow is assumed to be laminar with a surface velocity equal to the gas velocity immediately adjacent to the film's surface (Couette Flow): $u_f\left(y=+h\right)=U_g\left(y=+h\right)$. Since the gas phase and the liquid phase flows are computed separately, the interfacial shear stress provides a coupling between each phase, and an alternating iterative procedure is used to arrive at a converged solution.

The Rough Wall Model was proposed by Sattelmayer and Wittig [41] and the same research group has validated the model with time-averaged film thickness measurements [8,45]. The computational domain is two-dimensional, and the experimental test section of Wittig et al. [8,45] used to validate the model reduced three-dimensional effects constraining the film width to a distance equal to the width of the test

section. In Wittig et al. [8], it was stated that the test section design reduced any side wall effects on the film flow, so their study neglected any forces caused by film contact with the side wall. But, the flow duct used in the current study was wider than the film injection region, allowing the film width to change as the film propagates along the bottom wall. Therefore, the following analysis will validate the Rough Wall Model for simulating the current experimental facility.

Friedrich et al. [35] used the Rough Wall Model to simulate a water-surfactant film in the same test section as that used in this study. Their computational results for water-surfactant mixtures, which have a viscosity of 1.00 cP, can be applied to this study for vinegar, which also has a viscosity of 1.00 cP. Although the surface tension of vinegar (σ = 51 mN/m) is different than the surface tension of the water-surfactant mixtures used by Friedrich et al. [35] (σ = 26 mN/m, 42 mN/m), surface tension is not employed in the mathematical scheme of the Rough Wall Model and will not influence the results. Therefore, this study's experimental results of average film thickness and velocity were compared to the computations of Friedrich et al. [35]. Figures 4.37 and 4.38 show the results for average film thickness and velocity, respectively.

There are four specific trends revealed by these plots, and a discussion of these trends will begin by explaining those associated with film thickness. First, Figure 4.37 shows film thickness results for gas phase velocities of 20, 30, and 40 m/s, and high gas phase velocities resulted in thinner films, which was consistent with the experiments. More specifically, as gas phase velocity increased, then the change in film thickness became smaller. This trend was also consistent with the experiments, because the difference in film thickness for 30 and 40 m/s was smaller than the difference in film

thickness for 20 and 30 m/s. It is expected that film thickness would have limited sensitivity to a further increase in gas velocity. Second, and more importantly, the Rough Wall Model was inclined to over estimate film thickness. This inaccuracy was amplified at high film flow rates. At lower film flow rates though, when the experimentally measured film width was close to the film injection width ($w_f \approx w_{fo}$), the Rough Wall Model was most accurate. As explained in the Volume of Fluids model discussion, a two-dimensional model does not account for the increase in film width which took place at higher film flow rates. In the three-dimensional experiment, the film was thinner when allowed to spread across the bottom wall. This is a crucial element unconsidered by a two-dimensional model, but this dimensional conflict was thought to be avoided by plotting with a two-dimensional flow rate, $\frac{\dot{\forall}_f}{w_f}$, so there may be other problems with the Rough Wall Model methodology.

The third and fourth points of comparison were brought to light by the velocity results in Figure 4.38. Giving attention to film velocity with respect to film flow rate, the slope of these trends agreed well between simulations and measurements. Lastly, the Rough Wall Model was most accurate for high gas phase velocity situation. In fact, for U_g = 40 m/s the simulations have a mean error of only 4.4% when compared to measurements for the film flow conditions used in this study. To rationalize the increased accuracy occurring at high gas phase velocities, one should note that previous experimental validations of the Rough Wall Model used gas phase velocities of 30, 60, 90, 120, and 150 m/s [8,45]. This range showed agreement with simulated results, but it is with a gas velocity of 20 m/s that the current study exhibits large inaccuracies.

Figure 4.37. Average film thickness as simulated by the Rough Wall Model plotted with the experimentally measured values for vinegar.

Figure 4.38. Average film velocity as simulated by the Rough Wall Model plotted with the experimentally determined values for vinegar.

Combining the current study with the previous work of Wittig et al. [8,45], it appears that the Rough Wall Model is limited to average gas phase velocities above a certain minimum ($U_g \geq 30$ m/s). As mentioned in the earlier description of this model, the "wall roughness" methodology is a vital part of the simulation. Film surface structure is highly dependant on gas velocity, and the Rough Wall Model's mode of calculating the roughness constant may not properly capture the physics of lower gas velocities.

In conclusion, it should be reiterated that this study used a two-dimensional model to simulate an apparatus that allowed for three-dimensional effects. This problem was not revealed in the work of Wittig et al. [8,45] because the film width spanned from side wall to side wall for all flow conditions, and thus, the two-dimensional domain of the Rough Wall Model scheme is less likely to conflict with experiments. Intuitively, if side wall contact in the experiments of Wittig et al. [8,45] resisted film flow, then this would decrease film velocity and increase film thickness. This may be another reason why the Rough Wall Model is accurate when simulating the experiments of [8,45], but not as accurate for this study's experiments.

4.4. FILM SEPARATION MEASUREMENTS

4.4.1. Measurement Procedure. Film separation measurements were performed by removing liquid from the system if it remained attached to the bottom wall after the corner. This was done by drawing fluid through the porous brass drain located 6 mm after the corner. Figure 4.39 shows a picture of the test section, including the location of the porous surface. A pump provided negative pressure to transfer any liquid that remained

attached after the corner to a plastic bottle, where liquid was stored for mass measurement.

Figure 4.39. Picture of the test section showing the porous surface where the film that remains attached after the corner is removed.

One should give ample consideration to the arrangement used for drawing film from the system. Intuitively, if negative pressure is applied to an area located close to the corner then the separation process may be disturbed, engendering uncharacteristic behavior. This matter was given special attention in the facility design to confirm that the negative pressure caused by the liquid removal pump would not affect the film separation process. The film's behavior with and without a drain causing negative pressure was studied with high speed imaging at the corner. An example of this comparison is shown in Figure 4.40, where two images show the behavior of a film driven by a gas phase velocity of 40 m/s, and a volumetric film flow rate of 13.01 cm^3/s. The top image shows

film behavior in the corner section containing a drain with negative pressure and the lower image shows film behavior without the suction at the drain. Both images present the same general separation and break up behavior, where the ligaments have effectively the same length and thickness, confirming that the applying suction at a porous brass drain 6 mm from the corner will not disturb the separation process. Not all of the collected images appear exactly as shown in Figure 4.40, but these two images are an excellent representation of the general nature of film separation that was observed.

The film separation measurement procedure began with the start of liquid flow, switched on by the electromagnetic solenoid valve. For even the lowest liquid flow rates used in this study, the liquid film reached the corner within less than one second of switching on the valve. After the film flow reached the corner, the pump providing negative pressure at the porous brass drain was turned on. Immediately after the pump was turned on a valve between the pump and the drain was opened simultaneously with the start of a timer. At this point in the procedure, film was drawn out of the duct by the pump if the film remained attached to the bottom wall after passing the corner, and this liquid was stored in a bottle. Simultaneously, the valve was closed and the timer was stopped after approximately one minute, and then liquid flow was stopped using the solenoid valve. The procedure concluded by weighing the mass of the liquid captured in the storage bottle.

The total mass of liquid which flowed through the system was calculated using the volumetric film flow rate, fluid density, and time elapsed in the test, and this quantity was compared to the measured mass of liquid in order to find the mass percent of separated film. Combined uncertainty in this measurement is 5%.

Figure 4.40. High speed images for a surfactant-water mixture at a volumetric film flow rate of 13.01 cm^3/s, and a gas phase velocity of 40 m/s. (Top: with negative pressure applied at a drain 6 mm downstream from the corner; Bottom: without negative pressure)

4.4.2. Results. The Weber number is often used in correlations relating to break up and atomization due to its dependency on inertial forces and surface tension, both of which are paramount in these regimes. Film separation relies heavily on ligament break up and consequently, film separation results will be presented in a comparison with the film Weber number for each flow condition. Experimental film separation data is presented in Figure 4.41, which shows the mass fraction of separated film versus the film Weber number, We_f, where

$$We_f = \frac{\rho_f u_f^2 h_f}{\sigma}. \tag{15}$$

To calculate We_f for each flow condition, the experimental film thickness and velocity results presented in *4.3.2.2. Film thickness* and *4.3.2.3. Film velocity* were used, along with the fluid properties list in Table 4.1.

Figure 4.41 shows results for 48 different flow conditions, and the We_f corresponding to the onset of film separation is not clear. As gas velocity and film flow rate increased, the onset, or the point which film begins to separate, tended to occur at $We_f \approx 2$. Equally important, the effects of viscosity are shown by comparing $\mu_f = 1.00$ cP to $\mu_f = 1.42$ cP. The slope of the separation versus We_f relationship changed with a change in viscosity.

In accompaniment with the correlations mentioned above, one must note the parameters not accounted for by the Weber number. The Weber number is only a ratio of inertial forces and surface tension, and does not include film viscosity, gas velocity, or body forces. Therefore, the effects of film viscosity and gas velocity were only included within the film velocity and thickness, and any change in the corner angle, θ, was not considered. Conceptually, the corner angle will influence the amount of film separation at the corner, so a broader analysis should be explored in order to account for all governing parameters. In addition, although the Weber number provides a rough correlation for the increase in separation occurring at higher flow rates, it is not intended to be used as such. The Weber number does not provide a particular value at which the onset of film separation is expected to occur either. Within the physics of film separation,

Figure 4.41. Experimentally measured mass percent of film separation plotted versus the film Weber number for 43 flow conditions. The Weber number was calculated using experimentally measured values of film thickness and velocity.

there is an equilibrium which must occur for film to disconnect from the solid surface. A general flow parameter such as the Weber number does not incorporate this concept and should only be used as a comparison of inertial forces and surface tension.

4.4.3. Comparisons with Computational Models.

4.4.3.1. Force Ratio. Friedrich et al. [35] established a criterion for predicting the onset of film separation for a shear-driven film at a sharp corner. A force balance

approach was used to compare forces causing separation with forces acting to prevent separation. This force balance approach can be encompassed by the derivation of the resulting Force Ratio, which is described here.

To establish a working diagram, [35] drew a two-dimensional control volume around the liquid film, as shown in Figure 4.42, where a liquid film is at the point of separation and the film is forming a separating ligament at the corner. The formation of a

Figure 4.42. Force diagram of a film ligament at the point of separation. (Friedrich et al. [35])

suspended ligament was a noteworthy ingredient in the derivation of the Force Ratio, and its contribution will be discussed later in this section. A linear momentum conservation law was written for the control volume represented by dashed lines in Figure 4.42, where

the separating film within the control volume is at an angle of β from the horizontal. The bottom surface expands at an angle θ with the horizontal. Figure 4.42 shows the inertia of the film flow through the control volume, as well as surface tension forces and body forces acting at the boundaries of the control volume. These forces were balanced in the p-direction, perpendicular to the film. External forces considered were the surface tension force at the top of the film, F_s, the surface tension force at the bottom of the film, F_c, as well as a gravitational force, W. The surface tension forces acting at the downstream end of the ligament were not included because both are perpendicular to the p-direction. The surface tension force at the bottom of the film, F_c, was presumed to act perpendicular to the control surface, in the negative p-direction, at the meniscus between the separated liquid and the film that remains on the wall.

The gravitational force, W, along with both surface tension forces, F_c and F_s, were balanced with the film's inertia using the conservation of linear momentum for steady conditions for the p-direction,

$$\iint_{CS} \rho_f u_f \left(\vec{V} \cdot \vec{n}\right) dA = \rho \vec{g} \forall + \vec{F}_{ex} \quad . \tag{16}$$

Thus, the momentum flux through the control volume, represented by the left side of (16) was balanced with the gravitational force, $\rho \vec{g} \forall$, and the surface tension forces which compose $\vec{F}_{ex}$. By noting that there is no momentum flux exiting the control volume in the p-direction, (16) was expanded to attain

$$\rho_f u_f \dot{\forall}_f \sin\beta = w_f \sigma \sin\beta + w_f \sigma + \rho_f g h_f w_f L_b \cos\beta \tag{17}$$

where the momentum flux into the control volume in the p-direction was expressed as $\rho_f u_f \dot{\forall}_f \sin\beta$, and the surface tension and gravitational forces were expressed as $F_c = w_f \sigma$, $F_s = w_f \sigma \sin\beta$, and $W = \rho_f g h_f w_f L_b \cos\beta$. Substitution for $\dot{\forall}_f$ in equation (17) with

$$\dot{\forall}_f = u_f w_f h_f \tag{18}$$

and dividing by the film width resulted in a simplified version of (17):

$$\rho_f u_f^2 h_f \sin\beta = \sigma \sin\beta + \sigma + \rho_f g h_f L_b \cos\beta \tag{19}$$

As shown above, this force balance was written in terms of β, which is the angle of the separating ligament at the corner. At this point in the derivation, β was replaced by the corner angle, θ, in order to define the control volume at the onset of film separation. It was presumed that at the onset of film separation, or force equilibrium, the film at the corner will be at an angle $\beta = \theta$. The Force Ratio which results from this derivation, was intended as a calculation comparing forces causing film separation with forces inhibiting film separation, and follows as

$$Force\,Ratio = \left\{ \frac{\rho_f u_f^2 h_f \sin\theta}{\sigma \sin\theta + \sigma + \rho_f g h_f L_b \cos\theta} \right\} \tag{20}$$

Thus, the numerator of the Force Ratio is the inertial force causing film separation and the denominator consists of surface tension and gravitational forces, which prevent film separation. The gravitational force term includes a ligament length, L_b, which is calculated using an empirical relationship fashioned by Arai and Hashimoto [33]. This relationship follows as

$$L_b = 0.0388 h_f^{0.5}\, \mathrm{Re}_f^{0.6}\, We_{rel}^{-0.5} \tag{21}$$

where

$$We_{rel} = \frac{h_f \rho \left(U_g - u_f\right)^2}{2\sigma} \tag{22}$$

and

$$\mathrm{Re}_f = \frac{\dot{\forall}_f \rho_f}{w_f \mu_f} \ . \tag{23}$$

As shown by (20), a Force Ratio value of one is significant because the forces causing separation are equal to the restoring forces. Establishing the Force Ratio in this

manner allowed [35] to use Force Ratio calculations to predict the *onset* of film separation at a Force Ratio equal to one. Friedrich et al. [35] provided experimental film separation results to validate the Force Ratio as a film separation criterion, and the correlations were promising. The results provided verification not only that the onset of film separation occurs at a Force Ratio equal to one, but also that for higher values of the Force Ratio, the mass percentage of separated film follows an increasing trend common for all flow conditions.

There are two uncertainties to note regarding the work of Friedrich et al. [35]. First, to calculate the Force Ratio, film thickness and velocity at the corner was needed. This requirement was satisfied by predicting the film thickness and velocity using the Rough Wall film propagation model described in *4.3.3.2. Rough Wall Model.* In this format, inaccuracies in the Rough Wall Model's ability to predict film thickness and velocity will result in inaccuracies in the Force Ratio calculations. Secondly, their experiments were conducted over a wide range of flow conditions, but only two fluids were used. This allowed for investigation of surface tension effects, but not viscosity effects.

The current study performed further validation of the Force Ratio by using an improved set of testing conditions and by eliminating uncertainty in the film thickness and velocity at the corner. The improved test matrix includes three different fluids, allowing for variations in surface tension and viscosity. Also, uncertainties in the film thickness and velocity values used to calculate the Force Ratio were drastically reduced by using experimentally measured values instead of calculated predictions.

In Figure 4.43, film separation results are correlated to the calculated Force Ratio. Figure 4.43 represents the same set of measured results as Figure 4.41, but the film Weber number was replaced by the Force Ratio. As mentioned above, the film thickness and velocities used within the Force Ratio calculation are vital for the Force Ratio's accuracy, so it should be made clear that Figure 4.43 uses Force Ratio calculations established by the measured film thicknesses and velocities presented in *4.3.2.2. Film thickness* and *4.3.2.3. Film velocity*. First, one should note that the onset of film separation occurred at a Force Ratio slightly less than one, if not equal to one. This was true for all three fluids used in this study. Note the large error bars that occur for flow conditions exhibiting a low Force Ratio. The large uncertainties included at these low flow conditions resulted from the inability to remove all of the attached film from the test section. This uncertainty does not exist at high Force Ratio values due to the large amount of separation that takes place, which allows the porous drain to easily remove all of the film which remains attached after the corner. Experiments by Friedrich et al. [35] showed that the onset of film separation consistently occurred at a Force Ratio of one for various surface tension at μ_f = 1.00 cP. Therefore, the current study reaffirmed this conclusion and also demonstrated that a higher viscosity (μ_f = 1.42 cP) also results in a definitive onset of separation near one. Second, the slope of film separation versus the Force Ratio changed with film viscosity. For μ_f = 1.00 cP, the positive slope was greater than for μ_f = 1.42 cP. (General trend lines are shown in Figure 4.43). This may indicate that the Force Ratio does not properly incorporate the effect of viscosity on film separation. The Force Ratio included the effects of film viscosity in two ways; one directly, and one indirectly. First, film viscosity directly influenced the Force Ratio by its

Figure 4.43. Experimentally measured mass percent of film separation plotted versus the Force Ratio of Friedrich et al. [35] for 43 flow conditions. The Force Ratio was calculated using experimentally measured values of film thickness and velocity.

inclusion within the gravitational force term, or more specifically, the calculation of ligament length, L_b. An increase in film viscosity resulted in a decrease in L_b and thus a decrease in the gravitational force term. But proportionally, this effect was small due to the 0.6 exponential on Re_f in (21). Second, film viscosity indirectly influenced the Force Ratio through film velocity and thickness. For example, an increase in viscosity will generally cause a decrease in velocity and an increase in thickness. In the current

Figure 4.44. Experimentally measured mass percent of film separation plotted versus the Force Ratio of Friedrich et al. [35] for 43 flow conditions. The Force Ratio was calculated using values of film thickness and velocity predicted by the Volume of Fluids model.

experiment, the corner angle was fairly large ($\theta = 60°$), corresponding to a small gravitational force term. In fact, the gravitational term accounted for only 5 to 10% of the total force for the flow conditions used in this study. Ergo, the majority of the viscosity effect was not directly included by L_b within the gravitational force, but instead was indirectly included in the film thickness and velocity. Also, it should be reiterated that the oil film (μ_f = 1.42 cP, $\sigma = 27$ mN/m) made contact with the side walls due to a low

Figure 4.45. Experimentally measured mass percent of film separation plotted versus the Force Ratio of Friedrich et al. [35] for 16 flow conditions. The Force Ratio was calculated using values of film thickness and velocity predicted by the Rough Wall Model.

surface tension. If side wall effects are having a significant influence on oil film separation then this could be another cause of the differences in Figure 4.43.

To demonstrate the significance of the film thickness and velocity values used to calculate the Force Ratio, Figures 4.44 and 4.45 show the measured mass percent of film separation versus the Force Ratio, but the Force Ratio was calculated using CFD results. Figure 4.44 applied a Force Ratio calculated using film thickness and velocity values

from VOF model results, while Figure 4.45 applied a Force Ratio calculated using values taken from Rough Wall Model results. Comparing Figures 4.43, 4.44, and 4.45 manifests the salient differences between the Force Ratio calculated from measured film thickness as opposed to computational prediction. Viewing these three figures shows that for a given flow condition, the computational results of the VOF and Rough Wall Models elicit lower Force Ratio values than the experimental results. This shift occurs due to the over estimation of film thickness in the computational simulations, causing a smaller film velocity and thus a smaller inertial force term.

4.4.3.2. Radial Stress Model. A comparison was made of the Force Ratio with the work of Owen and Ryley [27], where a radial stress model was used to determine the onset of film separation. The three principle forces used in the Force Ratio are similar to the principle forces included in the radial stress model, where film inertia, surface tension, and body forces were used to estimate the radial stress of a film traveling on a rounded corner. In [27], the film was presumed as attached to the rounded corner with a specific radius and film thickness as shown in Figure 4.46. A positive radial stress in this case represented a compressive stress acting to keep the film attached to the wall. A negative stress was a tensile stress causing the film to separate from the wall. In each of the two force balance methods the principle forces included are the same, but further investigation shows significant differences within the terms of each method. These differences and their effects will be investigated further.

The inertial, gravitational, and surface tension force terms can be viewed individually. First, comparing the gravitational force terms within each force balance

Figure 4.46. Diagram for Radial Stress Model of Owen and Ryley [27].

gives rise to notable differences. These differences are caused by the use of a ligament length, L_b, in the Force Ratio model. The gravitational term used in the radial stress model does not treat the separating fluid as a ligament and therefore does not use a ligament length to determine the mass of the separating ligament. The characteristic ligament length in (21) includes liquid and gas properties and velocities within a liquid Reynolds number and a relative Weber number. The liquid Reynolds number includes film velocity, u_f, and film viscosity, μ_f, while the relative Weber number includes the gas phase velocity, U_g, film velocity, and surface tension, σ. None of these parameters are accounted for in the gravitational term used in the radial stress model because the fluid is analyzed as a particle, not a separated ligament. It should be noted that in the work of Friedrich et al. [35], high speed imaging methods were implemented to confirm the

formation of ligaments at the corner during the separation process. This was also shown by Figure 4.40.

Secondly, the surface tension force terms contained in each force balance method include different forces due to the characteristic ligament utilized in the Force Ratio model. In the radial stress model of Owen and Ryley [27], the particle of fluid of interest has surface tension forces acting in the direction of flow and against the direction of flow. In this case, both of these are slightly compressive forces due to the shape of the rounded corner. For the Force Ratio model, the force diagram in Figure 4.42 shows four surface tension forces, but two force vectors are shown at the downstream end of the ligament and do not possess a component in the p-direction. Therefore, the only two surface tension forces used in the Force Ratio include the force at the top surface of the film at the corner and the force at the lower meniscus. Both of these forces act in the negative p-direction to resist film separation. The force at the lower meniscus is not included in the radial stress model because the film is not viewed as a unique ligament. Consequently, like the gravitational term, the surface tension terms create significant differences between each separation criterion.

The radial stress model provides a criterion that greatly depends on film inertia. Figure 4.47 shows the relative influence of each term by plotting the percentage of the sum of all three terms for inertia, gravity, and surface tension. Over the flow conditions investigated here, film inertia is a large portion of the overall force, especially in the radial stress model, where the influence of gravity and surface tension becomes negligible at higher Re_f. The Force Ratio embodies a more evenly distributed force

Figure 4.47. Comparison of force balance contribution for the radial stress model of Owen and Ryley [27] (1) and the Force Ratio model of Friedrich et al. [35] (2) at U_g = 20 m/s.

balance. In fact, Figure 4.47 shows at Re_f = 160 the surface tension force is equal to the inertial force. These results clearly reveal the balance of forces determining the onset of film separation differ for each force balance method.

Similar to Figure 4.43, Figure 4.48 shows a plot of the mass percentage of separated film versus the radial stress of the Owen and Ryley model for each of the 43 different flow conditions. Comparing Figure 4.43 and Figure 4.48 confirms the significant differences that appear due to changing surface tension of the fluid. In Figure 4.48, different fluids provide different trends, showing a less robust correlation than Figure

4.43. Although the Force Ratio correlation did not provide the same trend for each fluid, the Force Ratio does appear to collapse the data better than the radial stress model. Also, the onset of film separation occurs at a radial stress of approximately -1000 N/m^2, but the radial stress model was derived such that the onset of separation should occur at zero, which elicits force equilibrium. The radial stress model's failure to predict the onset of film separation can be drawn back to the rudimentary approach to the problem, where the film was assumed to be completely attached or completely separated from the wall. Using high speed imaging, Friedrich et al. [35] showed this assumption to be false.

Figure 4.48. Experimentally measured mass percent of film separation plotted versus radial stress of Owen and Ryley [27] for 43 flow conditions. Radial stress was calculated using experimentally measured values of film thickness and velocity.

5. SUMMARY AND CONCLUSIONS

A study was made regarding liquid film separation, and more specifically, the experimental validation of film separation criteria. It was found that although there is a multitude of literature available concerning liquid films, such as thickness measurement, temperature measurement, and computational modeling, there are few previous studies which focus specifically on separation physics on either a theoretical and/or experimental basis. This study was meant to offer valuable shear-driven film separation data and present comparisons with available film separation criteria in a comprehensive manner, investigating the major uncertainties and variables involved.

An experimental facility was used to measure film separation at a sharp expanding corner for a wide range of flow conditions, allowing for a comparison with film separation criterion calculations for each flow condition. The experiment not only measured film separation, which is an extraordinary type of measurement, but also provided for the control or measurement of many other flow parameters. These included volumetric film flow rate, gas phase velocity, film viscosity, surface tension, film width, film velocity, and film thickness. In similar experiments, computational tools have been utilized as a way to predict the film velocity and thickness at the corner, and this method saves time and energy. But, this study optioned to use an experimental film thickness measurement technique to eliminate the uncertainty of relying on computational modeling accuracy.

The film thickness measurement technique utilized a laser focus displacement instrument. But, the instrument was first validated as a film thickness measurement tool, showing that the technique is accurate for measuring time-averaged film thickness and

not necessarily instantaneous film thickness. This conclusion was the fruit of an extensive investigation of the instrument that focused on surface angle limitations. It was found that due to light reflection physics, a laser focus displacement instrument is limited by the surface angle of the subject piece. The exact value of this surface angle limitation was desired in order to validate the instrument as a measurement tool for shear-driven liquid films, where dynamic wave structures can have large surface angles. Theoretically, the maximum measurable surface angle was estimated using the instrument's geometric specifications, the laser beam intensity distribution, and reflection coefficients according to the Fresnel equations. Experimentally, the maximum measurable surface angle was measured by coupling the instrument's thickness measurements with an image analysis technique for a static liquid drop. Ultimately, the surface angle limitation was found to be very significant, requiring that the subject surface be less than 6° from the horizontal. Although accuracy was not lost by increasing the angle from zero to 6°, the laser focus displacement instrument was unable to measure the interface location when the threshold of approximately 6° was reached. Thus, it was concluded that the LFD model used in this study was suited for measuring the peaks and valleys of waves on the surface of shear-driven films, but was not capable of measuring the steep surfaces between peaks and valleys. This limitation showed that the technique is accurate for measuring time-averaged film thickness and not necessarily instantaneous film thickness, or a film surface profile.

Using an LFD, time-averaged film thickness was measured for liquid films of three different fluids. The fluids chosen for this study allowed for isolation of film viscosity effects and surface tension effects. Also, five different volumetric film flow

rates were used with three different gas phase velocities to offer a broad test matrix. Compiling film thickness results for all flow conditions revealed that film thickness was affected most by volumetric flow rate and gas phase velocity and not fluid properties. This was true for the fluids used in this study, but may change for a greater variation in fluid properties. Film width measurements accompanied film thickness measurements, and average film velocity was inferred from the cross sectional area of the film determined using the width and thickness data.

The experimental film thickness and velocity measurements were then used to validate computational models. Two models were compared to the measured results. First, the Volume of Fluids model, which is part of the FLUENT Version 6.3 package, was described and used to simulate the experimental test section. Then, the same procedure followed for the Rough Wall Model, which is a numerical code devised specifically for modeling shear-driven films. Two-dimensional domains were used for each model, and there were salient difference between the experimental results and simulated results. It was concluded that the overlying cause of the discrepancies was the two-dimensional simplification of the simulations. The experimental apparatus allowed for three-dimensional flow effects such as changes in film width, while the two-dimensional models did not.

As a culmination of this study, all knowledge from the investigations listed above was compiled to decrease the uncertainties involved in film separation measurement. Film separation was measured and compared to the film Weber number and two theoretical film separation models in search of a robust theoretical prediction of the onset of film separation. The film separation models were calculated for each flow

condition using purely experimentally measured values, and then the same calculation was performed using the simulation results. The results of each method were compared, and it was found that the accuracies of the film thickness and velocity values are vital for separation model calculation. Thus, the laborious but valuable measurement of film thickness provided confidence in a sound calculation of separation models. One particular model, a force ratio balancing film inertia with surface tension and body forces, offered an accurate prediction of the onset of film separation for a film viscosity of 1.00 cP. Both models lacked the ability to collapse data from all fluids into a similar trend though.

6. RECOMMENDATIONS

To offer aid to any investigators that chose to perform a similar analysis or experiment, the recommendations discussed here have been divided into two main categories. The first includes changes to the analytical, or theoretical, portions of the study. The second is concerned with the experimental facility and flow conditions.

In the comparisons of film thickness and velocity between measured values and computer simulations, only two-dimensional simulations were used. There are three-dimensional models capable of modeling shear-driven films, and the experimental results should be compared with such a model. Actually, the Volume of Fluids model is fully capable of simulating a three-dimensional domain. This will simply require more computing time. It is also feasible to use the Rough Wall Model in a three-dimensional domain, but it would be quite labor intensive to rewrite the computer code to include a third dimension. A second recommendation for the analytical side of the study involves the laser focus displacement instrument validation. The theoretical prediction of the maximum measurable surface angle relied on several assumptions which could be eliminated if the laser beam's intensity profile is known. With an explicit beam intensity profile, one could use three-dimensional calculus to determine reflected light intensity as a function of subject surface angle. The relative power (P/P_o) strategy could still remain, but exact knowledge of the beam profile would eliminate the uncertainties within the relative power curve assumptions made in this study.

When an experiment involves a large number of variables, it is more difficult to create an apparatus which will allow for control of each variable. The test section used for this study placed limitations on several variables. The corner angle, θ, could be varied

to change the effects of gravity and surface tension on film separation, and changing the corner angle would require construction of a new corner section piece. Next, the entire test section's elevation angle could be altered, which would again change the effects of gravity on film separation. It is also recommended that the complete test section be as much as 75 mm wider and the top window should be expanded to cover the entire width of the test section. This would allow for complete optical access, and therefore, film thickness measurements across the entire width of the film. Also, a wider test section would prevent side wall contact for higher flow conditions, such as higher film flow rates and gas velocities. But, in order to reach higher gas phase flow rates, the liquid ring vacuum pump which drives flow must be replaced by a blower, which is better suited for moving large volumes of gas at ambient pressure. Another piece of equipment that may be changed is the laser focus displacement instrument. This instrument was previously available in a model with a larger beam cone angle than the model used for this study, which would provide for measurement of larger film surface angles. Although, a complete film surface profile would still not be measurable.

Last, it is recommended that a broader array of fluids be used. This study was the first of its kind to explore the effects of viscosity on the film separation process, but the change in viscosity was relatively small ($\Delta\mu_f = 0.42$ cP). Specifically, two fluids could be added to the test matrix. One would simply be water ($\mu_f = 1.00$ cP, $\sigma = 72$ mN/m) and one would be an aqueous glycerol solution, lending the capability of a high viscosity depending on the mass fraction of glycerol, while maintaining approximately the same surface tension as pure water. This would allow for a larger variation in film viscosity and surface tension. Although it is difficult to measure film width for fluids with very

high surface tension, the problems may be outweighed by the benefits. Also, concerning fluids with a high viscosity, there will be difficultly in removing large amounts of a thick, slow moving fluid. When removing the attached film from the test section, high viscosity fluids would definitely require a higher vacuum pressure to draw all of the attached mass from the test section. Even when using fluids with a viscosity of 1.00 cP as in this study, there was great difficulty in removing all of the attached film from the test section for flow conditions exhibiting a low Force Ratio value.

APPENDIX A.
DATA, DERIVATIONS, AND CODES

EXPERIMENTAL SURFACE TENSION MEASUREMENTS.

Surface tension was measured for each of the three fluids used in this study. A Kruess Processor Tensiometer Model K12 was used, and there was a 10 second interval between each measurement. The temperature specific for each set of measurements is noted next to the mean surface tension value.

Trial	Vinegar Surface Tension, σ_v (mN/m)	Glycerol-Vinegar Mixture Surface Tension, σ_{gv} (mN/m)	C-145 Oil Surface Tension, σ_{oil} (mN/m)
1	51.919	50.465	26.515
2	51.831	50.346	26.519
3	51.778	50.263	26.517
4	51.726	50.182	26.527
5	51.683	50.133	26.522
6	51.646	50.085	26.527
7	51.612	50.031	26.524
8	51.582	49.987	26.524
9	51.543	49.948	26.534
10	51.517	49.907	26.532
Mean	51.684 (20.6°C)	50.135 (20.4°C)	26.524 (20.1°C)

EXPERIMENTAL VISCOSITY MEASUREMENTS.

Viscosity was measured for each of the three fluids used in this study. The time required for the fluid to travel through a specific length of pipe is measured and then multiplied by a viscometer constant, which is unique for the viscometer used. Kinematic viscosity was calculated as the product of the elapsed time and the viscometer constant. Dynamic viscosity was calculated as the product of the kinematic viscosity and the fluid density. A Cannon-Ubbelohde Type Viscometer (Size 50 A880), which had a viscometer constant of 0.00385, was used. These measurements were made at room temperature, which was measured as 20.5°C.

Sample	Trial	Time, t (s)	Kinematic Viscosity, ν (cSt)	Dynamic Viscosity, μ (cP)
1	1	360.91	1.3895	1.4256
	2	356.34	1.3719	1.4076
	3	348.78	1.3428	1.3777
	4	354.06	1.3631	1.3986
	5	359.91	1.3857	1.4217
	6	358.59	1.3806	1.4165
	7	361.85	1.3931	1.4293
	8	364.56	1.4036	1.4400
2	1	363.78	1.4006	1.4370
	2	361.81	1.3930	1.4292
	3	361.53	1.3919	1.4281
	4	361.41	1.3914	1.4276
	5	356.78	1.3736	1.4093
	6	355.46	1.3685	1.4041
	7	368.06	1.4170	1.4539
	8	364.93	1.4050	1.4415
Mean		359.92	1.3857	1.4217

DERIVATION OF EQUATION (1).

- Find θ_R and θ_L

$$n_{air}\sin\left(\frac{\theta_C}{2}-\alpha\right)=n\sin(\theta_R)$$

$$\theta_R=\sin^{-1}\left[\frac{n_{air}}{n}\sin\left(\frac{\theta_C}{2}-\alpha\right)\right]$$

$$n_{air}\sin\left(\frac{\theta_C}{2}+\alpha\right)=n\sin(\theta_L)$$

$$\theta_L=\sin^{-1}\left[\frac{n_{air}}{n}\sin\left(\frac{\theta_C}{2}+\alpha\right)\right]$$

- Find α'

$$n_{air}\sin\alpha=n\sin\alpha'$$

$$\alpha'=\sin^{-1}\left[\frac{n_{air}}{n}\sin\alpha\right]$$

- Find $y'-x+x'$

$$\tan\alpha'=\frac{y'-x+x'}{h}$$

$$y'-x+x'=h\tan\alpha'$$

- Find y'

$$\sin\alpha=\frac{y'}{h'}$$

$$y'=h'\sin\alpha$$

- Find x'

$$\tan\left(\frac{\theta_C}{2}-\alpha\right)=\frac{x'}{h'\cos\alpha}$$

$$x'=h'(\cos\alpha)\tan\left(\frac{\theta_C}{2}-\alpha\right)$$

- Find x

$$\tan\theta_R=\frac{x}{h}$$

$$x=h\tan\theta_R$$

- Find h

$$y'-x+x'=h\tan\alpha'$$

$$h'\sin\alpha+h'(\cos\alpha)\tan\left(\frac{\theta_C}{2}-\alpha\right)-h\tan\theta_R=h\tan\alpha'$$

$$h'\left[\sin\alpha+(\cos\alpha)\tan\left(\frac{\theta_C}{2}-\alpha\right)\right]=h(\tan\alpha'+\tan\theta_R)$$

$$h=h'\frac{\sin\alpha+(\cos\alpha)\tan\left(\frac{\theta_C}{2}-\alpha\right)}{\tan\alpha'+\tan\theta_R}$$

$$h=h'\frac{\sin\alpha+(\cos\alpha)\tan\left(\frac{\theta_C}{2}-\alpha\right)}{\tan\left[\sin^{-1}\left(\frac{n_a}{n}\sin\alpha\right)\right]+\tan\left[\sin^{-1}\left[\frac{n_a}{n}\sin\left(\frac{\theta_C}{2}-\alpha\right)\right]\right]}=f(h',n_{air},n,\alpha,\theta_C) \qquad (1)$$

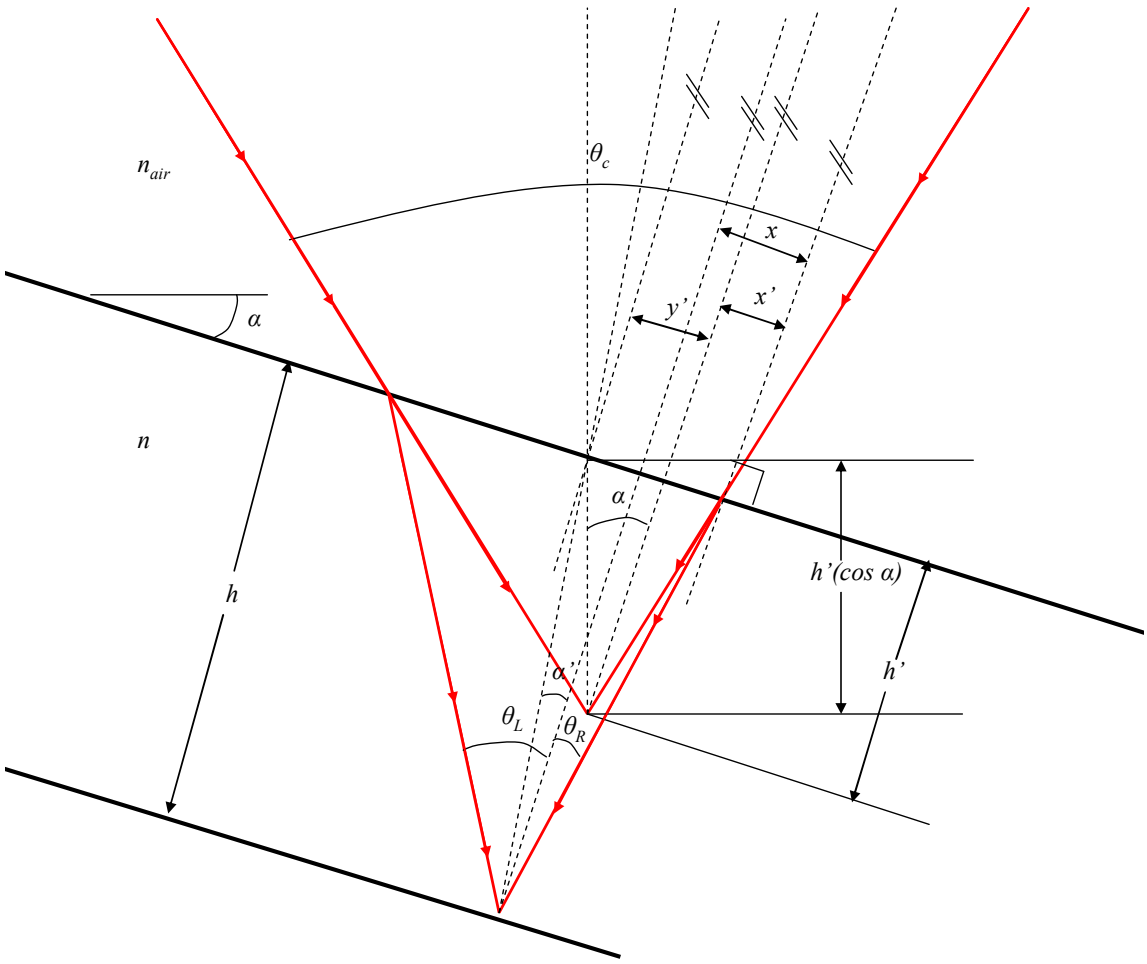

Figure A.1. Geometry for deriving Equation (1), which is used to calculate the thickness, *h*, of a specimen using the measured displacement of the top and bottom surface.

MATLAB CODE USED FOR LIQUID DROP IMAGE ANALYSIS.

```
IA = imread('Test_1A.bmp');
BW = im2bw(IA,.84);
imshow(BW);
pixval = 0;


%Find the bubble thickness.
for i=5:145
      surf(i)=35;
      for j=1:surf(i)
            pixval = impixel(BW,i,j);
            if (pixval > 0)
            surf(i)=j;
            end
      end
end

%Write the results to an excel file.
xlswrite('BubbleProfile.xls', surf(5:145), 'Sheet1', 'C3')
```

APPENDIX B.
EQUIPMENT AND FLUID SPECIFICATIONS

FLUID SPECIFICATIONS.

Oil:

Name	*Conosol*® C-145
Supplier	Penreco
CAS Number	64742-47-8
Kinematic Viscosity	1.76 cSt
Refractive Index	1.4442
Sulfur	<0.2 ppm
Pour Point	-70°F
Aromatics	<0.5% by weight
Density	0.80763 kg/L
Flash Point	152°F
Composition	by volume %
Saturates	>99
Olefins	<1
Aromatics	<1

Glycerol:

Name	*ReagentPlus*®, ≥99.0%
Supplier	Sigma-Aldrich
Synonyms	1,2,3-Propanetriol, Glycerin
CAS Number	56-81-5
Linear Formula	$HOCH_2CH(OH)CH_2OH$
Molecular Weight	92.09
Vapor Density	3.1 (vs air)
Vapor Pressure	<1mm Hg (20°C)
Autoignition Temperature	698°F
Refractive Index	1.474
Boiling Point	182°C
Density	1.25 g/mL
Flash Point	320°F

Vinegar:

Name	*Great Value*™ Distilled White Vinegar
Supplier	Wal-Mart Stores, Inc.
Strength	Diluted with Water to 5% Acidity
Intended Use	Ideal for Pickling
Linear Formula (Acetic Acid)	CH_3COOH
pH Value	2.4 to 3.4
Density	0.96 g/mL

LAMINAR FLOW ELEMENT CALIBRATION SPECIFICATIONS.

BIBLIOGRAPHY

[1] Hewitt, G. F., Measurement of Two Phase Flow Parameters, London: Academic Press, Inc., pp. 111-116, 1978.

[2] Ting, L. L., "Development of a Laser Fluorescence Technique for Measuring Piston Ring Oil Film Thickness," *J. of Lubrication Technology*, Vol. 102, pp. 165-171, 1980.

[3] Shaw II, B. T., Hoult, D. P., Wong, W., "Development of Engine Lubricant Film Thickness Diagnostics Using Fiber Optics and Laser Fluorescence," SAE 920651, 1992.

[4] Driscoll, D. I., Schmitt, R. L., Stevenson, W. H., "Thin Flowing Liquid Film Thickness Measurement by Laser Induced Fluorescence," *J. of Fluids Engineering*, Vol. 114, pp. 107-112, 1992.

[5] Yang, J., Melton, L. A., "Fluorescence-based Method Designed for Quantitative Measurement of Fuel Film Thickness during Cold-start Engines," *Society for Applied Spectroscopy*, Vol. 54, pp. 565-574, 2000.

[6] Maroteaux, F., Llory, D., Le Coz, J-F., Habachi, C., "Potential of Inertial Instabilities for Fuel Film Separation in Port Fuel Injection Engine Conditions," *International J. of Engine Res*., Vol. 4, pp. 11-26, 2003.

[7] Schagen, A., Modigell, M. "Local Film Thickness and Temperature Distribution Measurement in Wavy Liquid Films with Laser-induced Luminescence Technique," *Experiments in Fluids*, Vol. 43, pp. 209-221, 2007.

[8] Wittig, S., Himmelsbach, J., Noll, B., Feld, H. J., Samenfink, W. "Motion and Evaporation of Shear-driven Liquid Films in Turbulent Gases," *J. of Engineering for Gas Turbines and Power*, Vol. 114, pp. 395-400, 1992.

[9] Barter, J. D., Beach, K. L., Lee, P. H. Y., "Collocated and Simultaneous Measurement of Surface Slope and Amplitude of Water Waves," *Rev. Science Instrumentation*, Vol. 64, pp. 2661-2665, 1993.

[10] Barter, J. D., Lee, P. H. Y., "Real-time Wave-amplitude Spectrum Analyzer for Air-Liquid Interfaces," *Applied Physics Letters*, Vol. 64, pp. 1896-1898, 1994.

[11] Mouza, A. A., Vlachos, N. A., Paras, S. V., Karabelas, A. J., "Measurement of Liquid Film Thickness using a Laser Light Absorption Method," *Experiments in Fluids*, Vol. 28, pp. 355-359, 2000.

[12] Hurlburt, E. T., Newell, T. A., "Optical Measurement of Liquid Film Thickness and Wave Velocity in Liquid Film Flows," *Experiments in Fluids*, Vol. 21, pp. 357-362, 1996.

[13] Shedd, T. A., Newell, T. A., "Automated Optical Liquid Film Thickness Measurement Method," *Rev. Science Instrumentation*, Vol. 69, pp. 4205-4213, 1998.

[14] Samenfink, W., Wlsäßer, A., Wittig, S., Dullenkopf, K., "Internal Transport Mechanism in Shear-driven Liquid Films," *Proceedings of the Eighth International Symposium on Applications of Laser Techniques to Fluid Mechanics*, Lisbon, Portugal, 1996.

[15] Ohyama, T., Endoh, K., Atsushi, M., Mori, Y. H., "Optical Interferometry for Measuring Instantaneous Thickness of Transparent Solid and Liquid Films," *Rev. Science Instrumentation*, Vol. 59, pp. 2018-2022, 1998.

[16] Nosoko, T., Mori, Y. H., Nagata, T., "Improved Interferometer for Measuring Unsteady Film Thickness," *Rev. Science Instrumentation*, Vol. 67, pp. 2685-2690, 1996.

[17] Kelly-Zion, P., Collins, W., Glawe, D., "Application of Laser Interferometry for Transient Film Thickness Measurements," *Proceedings of 2004 ASME Heat Transfer/Fluids Engineering Summer Conference*, Charlotte, North Carolina, 2004.

[18] Friedrich, M. A., Lan, H., Wilke, N. E., Drallmeier, J. A., Armaly, B. F., "Measurement of the Mean Film Thickness of Dynamic Shear-driven Thin Liquid Films using Laser Interferometry," Submitted for acceptance in the *J. of Fluids Engineering*, 2008.

[19] Takamasa, T., Kobayashi, K., "Measuring Interfacial Waved on Film Flowing Down Tube Inner Wall using Laser Focus Displacement Meter," *International J. of Multiphase Flow*, Vol. 26, pp. 1493-1507, 2000.

[20] Takamasa, T., Hazuku, T., "Measuring Interfacial Waves on Film Flowing Down a Vertical Plate Wall in the Entry Region using Laser Focus Displacement Meters," *International J. of Heat and Mass Transfer*, Vol. 43, pp. 2807-2819, 2000.

[21] Busam, S., Ebner, J., Wittig, S., "An Experimental Study of Liquid Film Thickness in Annular Air/Oil Flow in a Vertical Pipe using a Laser Focus Displacement Meter," Presented at the *International Gas Turbine and Aeroengine Congress and Exhibition*, New Orleans, Louisiana, 2001.

[22] Hazuku, T., Takamasa, T., Okamoto, K., "Simultaneous Measuring System for Free Surface and Liquid Velocity Distributions using PIV and LFD," *Experimental Thermal and Fluid Science*, Vol. 27, pp. 677-684, 2003.

[23] Hazuku, T., Fukamachi, N., "Measurement of Liquid Film in Microchannels using a Laser Focus Displacement Meter," *Experiments in Fluids*, Vol. 38, pp. 780-788, 2005.

[24] Hazuku, T., Takamasa, T., Hibiki, T., Ishii, M., "Interfacial Area Concentration in Annular Two-phase Flow," *International J. of Heat and Mass Transfer*, Vol. 50, pp. 2986-2995, 2007.

[25] Hazuku, T., Takamasa, T., Matsumoto, Y., "Experimental Study on Axial Development of Liquid Film in Vertical Upward Annular Two-phase Flow," *International J. of Multiphase Flow*, Vol. 34, pp. 111-127, 2008.

[26] Hartley, D. E., Murgatroyd, W., "Criteria for the Break-up of Thin Liquid Layers Flowing Isothermally over Solid Surfaces," *International J. of Heat Mass Transfer*, Vol. 7, pp. 1003-1015, 1964.

[27] Owen, I., Ryley, D. J., "The Flow of Thin Liquid Films Around Corners," *International J. of Multiphase Flow*, Vol. 11, pp. 51-62, 1985.

[28] James, P. W., Azzopardi, B. J., Wang, Y., Hughes, J. P., "A Model for Liquid Film Flow and Separation in a Wave-plate Mist Eliminator," *J. of Chemical Engineering Research and Design*, Vol. 83, pp. 469-477, 2005.

[29] O'Rourke, P. J., Amsden, A. A., "A Particle Numerical Model for Wall Film Dynamics in Port-Injected Engines," SAE 961961, 1996.

[30] Maroteaux, F., Llory, D., Le Coz, J-F., Habachi, C., "Liquid Film Atomization on Wall Edges-Separation Criterion and Droplets Formation Model," *J. of Fluids Engineering*, Vol. 124, pp. 565-575, 2002.

[31] Gubaidullin, A., "Comments on 'Liquid Film Atomization on Wall Edges-Separation Criterion and Droplets Formation Model'," *J. of Fluids Engineering*, Vol. 129, pp. 665-666, 2007.

[32] Carvalho, I. S., Heitor, M. V., "Liquid Film Break-up in a Model of a Prefilming Airblast Nozzle," *Experiments in Fluids*, Vol. 24, pp. 408-415, 1998.

[33] Arai, T., Hashimoto, H., "Disintegration of Thin Liquid Sheet in a Concurrent Gas Stream," *Proceedings of the Third International Conference on Liquid Atomization and Spray Systems*, London, 1985.

[34] Steinhaus, B. C., Ghandhi, J. B., Shedd, T. A., "Experimental Investigation of Liquid Film Stripping at a Sharp Corner," *Proceedings of the 20th Annual Conference on Liquid Atomization and Spray Systems*, Chicago, Illinois, 2007.

[35] Friedrich, M. A., Lan, H., Wegener, J. L., Drallmeier, J. A., Armaly, B. F., "A Separation Criterion with Experimental Validation for Shear-driven Films in Separated Flows," *J. of Fluids Engineering*, Vol. 130, Issue 5, 051301, 2008.

[36] Hecht, E., Theory and Problems of Optics, McGraw Hill Book Co., pp. 40-41, 1975.

[37] Love, T. J., Radiative Heat Transfer, C.E. Merrill Publishing Co., pp. 55-68, 1968.

[38] Granados, K., Gracia-Fadrique, J., Amigo, A., Bravo, R., "Refractive Index, Surface Tension, and Density of Aqueous Mixtures of Carboxylic Acids at 298.15 K," *J. of Chemical Engineering Data*, Vol. 51, pp. 1356-1360, 2006.

[39] The Dow Chemical Company, "Refractive Index of Glycerine-Water Solutions at 20˚C (69˚F)," http://www.dow.com/glycerine/resources/table12_4160.htm, 2008.

[40] White, F. M., Viscous Fluid Flow, 3rd Edition, McGraw Hill Book Co., p. 22, 2006.

[41] Sattelmayer, T., Wittig, S., "Internal Flow Effects in Prefilming Airblast Atomizers: Mechanisms of Atomization and Droplet Spectra," *J. of Engineering for Gas Turbines and Power*, Vol. 108, pp. 465-472, 1986.

[42] Thiruvengadam, M., Armaly, B. F., and Drallmeier, J. A., "Shear-driven Liquid Film in a Duct: Comparison with Measured Results," *Proceedings of the ASME International Mechanical Engineering Congress and Exposition*," Chicago, Illinois, 2006.

[43] Buelow, P. E. O., Mao, C. P., Smith, S., and Bretz, D., "Application of Two-phase CFD Analysis to a Prefilming Pure-airblast Atomizer," *Proceedings of the 37th AIAA/ASME/SAE/ASEE Joint Propulsion Conference*, Salt Lake City, Utah, pp. 1-10, 2001.

[44] Lan, H., Friedrich, M. A., Armaly, B. F., and Drallmeier, J. A., "Simulation and Measurement of 3D Shear-driven Thin Liquid Film in a Duct," *International J. of heat and Fluid Flow*, Vol. 29, pp. 449-459, 2008.

[45] Himmelsbach, J., Noll, B., and Wittig, S., "Experimental and Numerical Studies of Evaporating Wavy Fuel Films in Turbulent Air Flow," *International J. of Heat and Mass Transfer*, Vol. 37, pp. 1217-1226, 1994.

VITA

Jeffrey Lewis Wegener was born in Lenexa, Kansas, USA on February 5, 1985 and was raised in Raytown, Missouri, a suburb of Kansas City. At a young age, he showed great interest in all things mechanical, which was stimulated and encouraged by his father and grandfather. Jeff graduated from Raytown High School in 2003 and then enrolled at University of Missouri-Rolla. As an undergraduate, he became a member of Sigma Phi Epsilon Fraternity, where he served as president in 2006. In October of 2006, Jeff was a runner-up for UMR Homecoming King and Interfraternity Council Man of the Year. He worked as an engineering intern for Deere and Company for 3 summer terms in Iowa, and was an undergraduate research assistant in the internal combustion engine laboratory under Dr. James A. Drallmeier. Jeff graduated with a Bachelor of Science degree in Mechanical Engineering in August of 2007 and immediately began graduate work in Mechanical Engineering under the advisement of Dr. Drallmeier. After completing his Master of Science degree in May of 2009, he will work at Edwards Air Force Base, CA for the U.S. Air Force Research Laboratory in a temporary position as a propulsion rocket scientist. He plans to begin work towards a PhD in autumn of 2009. Aside from engineering, Jeff enjoys fishing, baseball, football, and spending time with his family and friends.